

INTEGRAL FIELD SPECTROSCOPY OF THE LUMINOUS INFRARED GALAXY ARP 299 (IC 694+NGC 3690)¹

M. GARCÍA-MARÍN², L. COLINA², S. ARRIBAS^{3,4,5}, A. ALONSO-HERRERO², E. MEDIAVILLA⁵

Draft version February 4, 2008

ABSTRACT

The luminous infrared galaxy Arp 299 (IC 694+NGC 3690) is studied using optical integral field spectroscopy obtained with the INTEGRAL system, together with archival *Hubble Space Telescope* WFPC2 and NICMOS images. The stellar and ionized gas morphology shows λ -dependent variations due to the combined effects of the dust internal extinction, and the nature and spatial distribution of the different ionizing sources. The two-dimensional ionization maps have revealed an off-nuclear conical structure of about 4 kpc in length, characterized by high excitation conditions and a radial gradient in the gas electron density. The apex of this structure coincides with B1 region of NGC 3690 which, in turn, presents Seyfert-like ionization, high extinction and a high velocity dispersion. These results strongly support the hypothesis that B1 is the true nucleus of NGC 3690, where an AGN is located. In the circumnuclear regions H II-like ionization dominates, while LINER-like ionization is found elsewhere. The H α emitting sources with ages from 3.3 to 7.2×10^6 years, have masses of between 6 and $680 \times 10^6 M_{\odot}$ and contribute (extinction corrected) about 45% to the bolometric luminosity. The ionized (H α) and neutral (NaD) gas velocity fields show similar structure on scales of several hundred to about 1 kpc, indicating that these gas components are kinematically coupled. The kinematic structure is complex and on scales of about 0.2 kpc does not appear to be dominated by the presence of ordered, rotational motions. The large velocity dispersion measured in NGC 3690 indicates that this galaxy is the most massive of the system. The low velocity amplitude and dispersion of the interface suggest that the ionized gas is slowly rotating or in a close to quiescent phase.

Subject headings: galaxies: individual (Arp 299, IC 694, NGC 3690) — galaxies: interaction — galaxies: starburst — galaxies: nuclei — galaxies: stellar content — galaxies: kinematics and dynamics — infrared: galaxies

1. INTRODUCTION

Arp 299 is a nearby luminous infrared galaxy ($d \sim 43$ Mpc for $H_0 = 70$ km s⁻¹Mpc⁻¹, $\Omega_M = 0.7$, $\Omega_{\Lambda} = 0.3$) with an infrared (8-1000 μ m) luminosity of $L_{IR} = 5.7 \times 10^{11} L_{\odot}$ ⁶. It is an interacting system (Fig. 1) composed of two individual galaxies (IC 694+NGC 3690⁷) in an early dynamical stage. Hibbard & Yun (1999) have discovered an H I tidal tail of 180 kpc in length, with no evidence for tidal dwarf galaxies. Powerful starburst regions with star formation

rates of up to about $100 M_{\odot} \text{ yr}^{-1}$ have been identified (Alonso-Herrero et al. 2000, hereafter AAH00). Moreover, the system presents several regions where supernova remnants have been detected at radio wavelengths (Neff et al. 2004). More recently, Mattila et al. (2005) have discovered a new supernova using near-IR images, reinforcing the prediction that this galaxy has a high rate of supernova explosions (Mannucci et al. 2003).

Optical spectroscopic studies have classified IC 694 as starburst, and NGC 3690 as starburst/LINER (e.g., Coziol et al. 1998), and mid-IR observations classified the system as starburst (e.g., Laurent et al. 2000). Using *Hubble Space Telescope* (HST) imaging and near-infrared spectroscopy, AAH00 modeled the star formation properties of the system without the need for an AGN. The first hint for the presence of an AGN in Arp 299 came from X-ray observations with the *BeppoSAX* satellite by Della Ceca et al. (2002). These authors concluded that a highly absorbed ($N_H \simeq 2.5 \times 10^{24} \text{ cm}^{-2}$) AGN, with an intrinsic luminosity of $L_{0.5-100 \text{ keV}} \simeq 1.9 \times 10^{43} \text{ erg s}^{-1}$, is present in this galaxy, although due to the low spatial resolution its exact location could not be determined. Using *Chandra* and *XMM-Newton* observations, recent studies (Ballo et al. 2004) have inferred the presence of two AGNs, one located in NGC 3690 (source B1; 6.4 keV line), and another in IC 694 (source A; 6.7 keV Fe-H α line). In addition, Gallais et al. (2004) suggest the presence of an AGN in NGC 3690 based on the shape of the mid-IR continuum, while in IC 694 they only detect spectral features characteristic of massive, dust enshrouded star formation.

¹ Based on observations with the William Herschel Telescope operated on the island of La Palma by the ING in the Spanish Observatorio del Roque de los Muchachos of the Instituto de Astrofísica de Canarias. Based also on observations with the NASA-ESA Hubble Space Telescope, obtained at the Space Telescope and Science Institute, which is operated by the Association of Universities for Research in Astronomy, Inc. under NASA contract number NAS5-26555.

² Departamento de Astrofísica Molecular e Infrarroja, Instituto de Estructura de la Materia, CSIC, E-28006 Madrid, Spain.

³ Space Telescope Science Institute, 3700 San Martin Drive, Baltimore, M.D. 21218, USA.

⁴ On leave from the Instituto de Astrofísica de Canarias (IAC) and from the Consejo Superior de Investigaciones Científicas (CSIC), Spain.

⁵ Instituto de Astrofísica de Canarias (IAC), 38205 La Laguna, Canary Islands, Spain.

⁶ IRAS fluxes obtained from Moshir et al. (1993). L_{IR} derived from the equation detailed on Sanders & Mirabel (1996).

⁷ Through this paper, we use the notation introduced by Gehrzt et al (1983) for the two components of Arp 299: the nucleus of IC 694 (eastern component) is region A, while the main sources in NGC 3690 (western component) are B1, B2, C(C1+C2+C3) and C' (see also Alonso-Herrero et al 2000).

This paper presents a detailed study of the two-dimensional star formation, kinematics, and ionized gas properties of Arp 299, covering the two individual galaxies of the system and the interface area. At a distance of about 43 Mpc, Arp 299 is one of the nearest interacting, luminous infrared galaxies, and therefore these observations provide high spatial resolution (about $0.205 \text{ kpc arcsec}^{-1}$) and allow us to investigate in detail the structure and physical properties of this galaxy. The paper is organized as follows: §2 describes the observations and data reduction, while the selection of regions under study is described in §3. The next sections present a discussion of the results, with special emphasis on the stellar and ionized gas morphology (§4), the internal dust distribution and extinction effects (§5), the extinction estimates using optical and near-IR emission lines (§5.4), the two dimensional ionization structure (§6), the electron density (§7), the origin of the LINER-like ionization (§8), the star-forming properties (§9), and the kinematics and dynamical mass derivations (§10). Finally §11 presents a short summary of the main new results.

2. OBSERVATIONS AND DATA REDUCTION

Integral Field Spectroscopy (IFS) of Arp 299 was obtained on 2004 January 15 and 17 using INTEGRAL, a fiber-based integral field system (Arribas et al. 1998) connected to the Wide-Field Fiber Optic Spectrograph (WYFFOS) (Bingham et al. 1994) and mounted on the 4.2 m William Herschel Telescope. Two different INTEGRAL configurations were used for observing the system (see pointings in Fig. 1). The fiber bundle with the largest field of view (FoV), SB3, was centered on a position equidistant from the centers of the galaxies and therefore used to map the diffuse, interface region between the two galaxies (IC 694+NGC 3690) that form the Arp 299 system, as well as the galaxy external regions at distances of about 4 kpc. The SB3 bundle consists of 115 fibers each $2''.7$ in diameter, covering a rectangular area of $33''.6 \times 29''.4$ on the sky. In addition 20 fibers, forming a circle of $45''.0$ in radius, were used to obtain a spectrum of the sky simultaneously. The SB2 bundle was used to map each of the two galaxies (IC 694 and NGC 3690, eastern and western galaxies, respectively on Fig. 1) individually. It consists of 189 fibers each $0''.9$ in diameter, covering a rectangular area of $16''.0 \times 12''.3$ on the sky. In addition 30 fibers, forming a circle of $45''.0$ in radius, were used to measure the sky simultaneously.

The spectra were taken using a $600 \text{ lines mm}^{-1}$ grating, with an effective spectral resolution (FWHM) of approximately 6.0 \AA and 9.8 \AA for the SB2 and SB3 bundles respectively, and covering the spectral range $\lambda\lambda 4400\text{--}7000 \text{ \AA}$. The total integration time was 3600 s for each pointing with the SB2 bundle, split into three individual exposures of 1200 s each. The total integration time with the SB3 bundle was 5400 s divided into three individual exposures of 1800 s each. The seeing conditions were fairly stable during the two periods of observation (about $0''.7$ the first night, when we used the SB2 bundle, and $1''.1$ the second night when we used the SB3 bundle).

The data reduction consists of three main steps: 1) the basic reduction of two dimensional fiber spectra, 2) the line fitting, and 3) the generation of maps of spectral features (such as intensity maps and velocity fields) from the calibrated spectra. The basic reduction was performed

using the IRAF⁸ environment, and followed the standard procedures applied to spectra obtained with two-dimensional fiber spectrographs (Arribas et al. 1997 and references therein). The absolute flux calibration was performed observing the standard star Feige 34 with the same instrument configuration and data reduction procedures used on the galaxy. For each spectrum, the total flux, the radial velocities and the velocity dispersions (σ) were measured by fitting single Gaussian functions to the observed emission line profiles using the DIPSO package (Howarth & Murray 1988). For the generation of the maps, a two dimensional interpolation was applied using the free software IDA (García-Lorenzo et al. 2002). The blue and red stellar continuum images were taken as an emission line-free filter centered at $\lambda_{restframe}=4475 \text{ \AA}$ and 6525 \AA respectively, and with a rectangular bandwidth of 150 \AA . The measures on the SB3 maps were done through an aperture of $3''.0$ in diameter, while for the SB2 maps the apertures diameter were $1''.0$ (IC 694) and $0''.9$ (NGC 3690, to avoid the overlap between regions).

Three sample spectra, covering the entire used spectral range, are shown in Fig. 2. All the spectra show the strong ($H\beta$, $[O III]\lambda\lambda 4959, 5007$, $H\alpha + [N II]\lambda\lambda 6548, 6584$, $He I\lambda 6678$, and $[S II]\lambda\lambda 6716, 6731$) and the weak ($N I\lambda 5199$, $He I\lambda 5876$, $[O I]\lambda\lambda 6300, 6364$, and $He I\lambda 6678$) emission lines in different ratios, as well as interstellar absorption lines ($Na I\lambda\lambda 5890, 5896$), that will be used to trace the neutral interstellar medium kinematics.

Complementary HST multiwavelength images both in continuum and emission lines are also available. These additional data include the red (WFPC2-F814W, archive images) and the near-infrared (NICMOS1-F110M, NICMOS2-F160W and NICMOS2-F222M, from AAH00) continuum images. These filters are the HST equivalent to the ground-based Johnson-Cousins system *I*, *J*, *H* and *K* respectively (Origlia & Leitherer 2000). Images of the ionized gas as traced by the $P\alpha$ ($\lambda_{rest}=1.875 \mu\text{m}$) light (NICMOS-F190N, from AAH00) will be used too. The archival WFPC2 image was calibrated on-the-fly with the best available reference files, while the NICMOS images were reduced with routines from the package NicRed (McLeod 1997; see details on AAH00).

3. SELECTION OF REGIONS UNDER STUDY

In order to analyze the system we have selected several regions distributed over the individual galaxies, the interface between them and regions external to the galaxies (Fig. 1). The selection includes compact unresolved high-surface brightness knots, star clusters and more diffuse, extended resolved low-surface brightness areas. For IC 694 and NGC 3690 we based our selection on that done by AAH00, that includes the nuclear regions (A and B1 respectively) and the most important star-forming regions and bright star clusters. To identify the position of the regions under study in the lower resolution INTEGRAL maps, a direct comparison of the convolved WFPC2 image with the red continuum image was performed. The following sections present the main results

⁸ IRAF software is distributed by the *National Optical Astronomy Observatories (NOAO)* which is operated by the *Association of Universities for Research in Astronomy, Inc. (AURA)* in cooperation with the *National Science Foundation*.

obtained for these different regions and discuss their implications separately for the two individual galaxies, IC 694 and NGC 3690, and for the interface region between them. The physical properties measured for each individual region are presented in Tables 1 to 3.

4. STELLAR AND IONIZED GAS MORPHOLOGY

Arp 299 is the result of a merger between the galaxies IC 694 and NGC 3690, whose nuclei (A and B1 respectively, see Fig. 3) are located about 4.6 kpc apart. The system shows a morphologically disturbed structure characterized by the presence of compact high-surface knots, and a complex system of filaments and dust lanes, as already indicated by previous studies at several wavelengths (e.g. Gerhz et al. 1983; Telesco et al. 1985; Baan et al. 1990; AAH00). In what follows, we discuss the differences in the spatial distribution of the stellar and ionized gas components.

4.1. Interface Region

The two INTEGRAL/SB3 continuum images of Arp 299, obtained at wavelengths blueward of $H\alpha$ and $H\beta$, reproduce well the overall stellar morphology detected with the HST WFPC2 F814W image (Fig. 3) although at a lower spatial resolution (fiber diameter $2''/7$, scales of $\simeq 0.5$ kpc). In spite of that, the interface region between the two galaxies, and the external regions show well defined features such as the bridge to the south of region K5 connecting NGC 3690 and IC 694, and the elongated emission connecting K1 towards K12 source as part of a tail-like structure located to the SW of NGC 3690 (see Fig. 1).

The general structure of the low surface brightness ionized gas in the interface region, as traced by for example $H\alpha$ (Fig. 3), is similar to that of the stellar component. However, several differences exist. Diffuse ionized gas is detected NE of NGC 3690, associated with the K5 and C' knots; the latter region shows $\text{Pa}\alpha$ emission and SN activity in radio (Neff et al. 2004), and is part of a bridge of ionized material (see Fig. 3, $H\alpha$ map) to the north of the stellar bridge that connects the two individual galaxies. The $[\text{O III}]\lambda 5007$ emission map presents an elongated structure located towards the south-east of B1 and B2 tracing an area where the ionized gas presents high excitation state (see §6.1). However, as showed in the next two sections, the most important morphological variations are associated to the main bodies of the galaxies when observed with the higher angular resolution SB2 bundle.

4.2. IC 694

Previous studies have concluded that IC 694 was a spiral galaxy that due to the merging process shows a more disrupted morphology (e.g., Gerhz et al. 1983; Stanford & Wood 1989; Hibbard & Yun 1999). The stellar structure as seen from both the HST and the INTEGRAL continuum images (see Fig. 4) is divided into two main substructures: (1) The arm (region centered around A7) of about 1.8 kpc in length, that could be one of the original spiral arms disrupted and deformed as a consequence of the merging-process, and (2) the main body of the galaxy, formed by the dust-enshrouded infrared nucleus A (AAH00), and surrounding regions. The two structures are well separated (distances of $\simeq 1$ kpc) by what

seems to be a dust lane, that is clearly visible in the HST near-IR color maps (AAH00). The effect of the internal extinction is remarkable in the continuum images as the relative surface brightness of the regions, in particular nucleus A and surrounding regions, changes with wavelength (see Fig. 4 and discussion in §5.2).

The ionized gas distribution (see Fig. 4) shows several distinct features worth mentioning. The nucleus of the galaxy (A) appears as a weak optical line emitting source, whereas the regions of high surface brightness are located at different positions (e.g., part of the arm and towards east, and regions close to A) and separated up to 1 kpc from the nucleus. However, in the near-IR A is the brightest $\text{Pa}\alpha$ and $\text{Br}\gamma$ source (see AAH00 and Sugai et al. 1999, see also §5.2), indicating that the extinction towards the nucleus is very high (using $\text{Pa}\alpha/H\alpha$ ratio, $A_V = 6.1 \pm 0.7$). There are regions (e.g. knot G) that appear as a faint continuum sources, but that are clearly identified as strong optical line emitters. In addition to differences in the morphology of the ionized gas (i.e. excitation conditions) with respect to that of the continuum, there are also differences in the ionized gas distribution as traced by several lines. The hydrogen recombination lines and the $[\text{N II}]\lambda 6584$ and $[\text{S II}]\lambda \lambda 6717, 6731$ emission lines show a similar distribution, dominated by the emission from regions located on the arm and towards the east, and in the regions surrounding the nucleus. However, the shock tracer $[\text{O I}]\lambda 6300$ line is concentrated in region H1, while the higher excitation line $[\text{O III}]\lambda 5007$ appears to be brightest in regions A7 and G. These differences in the distribution of the emission line gas are not only due to internal extinction effects, but they also reflect changes in the ionization conditions as a function of location within the galaxy (see §6.1).

4.3. NGC 3690

The stellar light distribution as observed with the HST shows an irregular morphology dominated by the emission coming from the high surface brightness region B2 (identified therefore as the optical nucleus), and from region B1 and complex C⁹ located at distances of 0.49 and 1.3 kpc from B2, respectively (see Fig. 5). However at near and mid-IR wavelengths the true nucleus of the galaxy (see discussion in §10.2), B1, becomes the brightest continuum region in NGC 3690 (see AAH00; Satyapal et al. 1999). This disordered morphology could be the combination of the original spiral structure with young star-forming regions such as the complex C, and regions D3 or C', newly formed as a consequence of the interaction process as suggested by several authors (e.g. Gerhz et al. 1983; Stanford & Wood 1989; Baan & Haschick 1990; Hibbard & Yun 1999).

The distribution of the ionized gas (Fig. 5) is simpler than that of IC 694. The optical nucleus (B2) appears as an extremely faint line emitter, and the structure of the ionized gas is dominated by two high surface brightness regions separated by 1.8 kpc, nucleus B1 and the complex C (with the peak located towards C2), as previously founded with near-IR hydrogen recombination lines (Sugai et al. 1999; AAH00). The bright-

⁹ As explained in Note 7, we will use the term complex C introduced by Gehrz et al. (1983) for the regions C1, C2 and C3 (see Fig. 1).

est emission line peak is associated to C2 for all lines but the shock tracer [O I] λ 6300. For the latter, the nucleus B1 is the brightest emitter, as also observed with the near-IR [Fe II] λ 1.64 μ m line (AAH00). Analyzing in detail the secondary emission line peaks associated to B1 and surrounding areas, it is interesting to note that the high excitation [O III] λ 5007 emission is dominated by B1, while the H α and H β emission peaks are associated to region B16 (which is located 0.26 kpc southwest of B1, and identified in the λ 4475 continuum map). Low excitation collisional lines [N II] λ 6584, [S II] λ 6717, 6731 appear to have secondary peaks in both B1 and B16. These changes in the emission line distribution represent changes in the ionization conditions, and most likely in the ionizing source (AGN, young stellar clusters and shocks) on scales of less than 0.3 kpc.

5. INTERNAL DUST DISTRIBUTION AND EXTINCTION EFFECTS

As mentioned in the previous section, part of the complex structure observed in the continuum and emission line light distributions is due to large amounts of dust producing spatially dependent internal extinction effects. The two dimensional extinction maps of the gas (Figs. 6, 7 and 8) have been derived using the H α /H β line ratio, a foreground dust screen model, and a mean interstellar extinction law based on that of Savage & Mathis (1979). No correction for the presence of underlying stellar hydrogen absorption lines has been applied. Assuming an equivalent width value of $EW_{abs}(H\alpha) = EW_{abs}(H\beta) \sim 2 \text{ \AA}$, the derived extinction could be overestimated by as much as $\Delta E(B-V) \sim 0.6$ for regions with extremely faint H β emission (e.g. $EW(H\beta) \leq 20 \text{ \AA}$). The values for the visual extinction ($A_V = 3.1 \times E(B-V)$) in particular regions are given in Tables 1, 2, and 3. The results suggest that the highest extinguished regions are, in general, associated to the nuclei and some particular regions (like C'), while the external H II regions are mostly less affected by the presence of dust.

5.1. Interface Region

The extinction in the whole area covered by the SB3 bundle on scales of about 3''0 (i.e. 0.6 kpc), is relatively uniform (see Fig. 6). It has an average value of $A_V = 1.9$ mag on the selected individual regions, and ranges from $A_V(K2) = 0.9 \pm 0.7$ mag to $A_V(K5) = 2.9 \pm 0.7$ mag (see Table 1 for specific values on all the individual regions).

5.2. IC 694

On scales of about 1''0 (i.e. 0.21 kpc), the internal extinction in the visual covers a wide range of values from about $A_V = 0.6 \pm 0.5$ mag in the southwestern section of the galaxy to $A_V = 3.4 \pm 0.5$ mag in region H2, close to the nucleus A (see Table 2 for specific values, and Fig. 7 for the two dimensional E(B-V) distribution). As can be seen from Fig. 7, the H α extinction corrected light distribution shows an overall structure similar to that of the Pa α line except for the region associated with the peak of the emission. While the nucleus A, identified as the brightest near-infrared source in the HST images (Fig. 7, see also AAH00), is also the dominant Pa α line emitter, the peak of the extinction corrected H α distribution is located in regions H1 and H2, 0.3 and 0.5 kpc towards

the east of the nucleus. Also region F, located 1.58 kpc to the south-east of A, appears as a strongly absorbed region ($A_V = 3.2 \pm 0.5$ mag), and as a strong H α emitter after correcting for extinction. Additional secondary H α sources are mostly associated with star-forming regions (the arm, a region towards the west of A) at distances of 1 to 1.6 kpc from the nucleus, and delineating what seems to be a spiral-like arm structure previously identified in the Pa α emission line map.

5.3. NGC 3690

This galaxy presents the widest range of extinction (derived from the H α /H β ratio) for the entire Arp 299 system with values that for the individual regions range from $A_V(C4) = 0.5 \pm 0.5$ mag to $A_V(B2) = 3.9 \pm 0.6$ mag (see Table 3). Also, the nucleus B1 in this galaxy is the region of the Arp 299 system which has associated the highest H α /H β -based extinction, $A_V \simeq 4.6$ mag (Fig. 8).

The overall structure of the extinction corrected H α line distribution agrees well with that of the Pa α line (Fig. 8, see also AAH00) not only on the high surface brightness regions such as the nucleus B1 and C1, but also on the low surface brightness region, including B2 identified as the optical nucleus.

5.4. Extinction estimate using optical and near-IR emission lines

Additional line ratios involving IR hydrogen recombination lines (e.g., Pa α /H α , Br γ /Pa α , and Pa α /Pa β), can provide better estimates of the internal extinction in highly extinguished regions as those identified in Arp 299 (see Table 4).

The Pa α image of the individual galaxies (see Figs. 7, 8, and AAH00) has been used for measuring all the regions under study with apertures of 1''0 for IC 694 and of 0''9 for NGC 3690 to match our ground-based apertures; the INTEGRAL H α fluxes are given in Tables 2 and 3. In most regions extinction estimates based on only optical and optical+infrared lines agree within the uncertainties (Table 4). On the other hand, there are two regions, the nucleus of IC 694 (A) and C', where the use of the optical+infrared lines indicates a larger extinction than using only the optical lines, i.e. $A_V(\text{Pa}\alpha/\text{H}\alpha) \simeq 2 \times A_V(\text{H}\alpha/\text{H}\beta)$. This means that the extinctions derived using the H α /H β ratio are in general consistent with the ones derived using the Pa α /H α ratio, except in highly absorbed regions, where there is an underestimate when only the optical lines are used. These extinctions are similar with those measured in the M51 nuclear H II regions (Calzetti et al. 2005), and in other LIRGs (Alonso-Herrero et al. 2006) using the same near-IR/optical emission lines.

6. TWO-DIMENSIONAL IONIZATION STRUCTURE

The ionization level for the individual regions identified in Arp 299 has been derived using standard optical emission line diagnostic diagrams (BPT diagrams: Baldwin, Phillips & Terlevich 1981; Veilleux & Osterbrock 1987). H II-like ionization (i.e. star formation) is present on the majority of the regions of the individual galaxies, except for nucleus B1 which clearly has Seyfert-like (i.e. presence of an AGN) state. LINER-like ionization is mainly present on the interface (Fig. 9; see also Tables 1, 2, and 3 for specific values of the emission line ratios). Several

regions show changes in the classification depending on the specific diagram used; these variations have been interpreted as a consequence of changes in the dominant ionizing mechanism from photoionization to shocks (e.g. Monreal-Ibero et al 2006 and references therein). In particular, the $[\text{O III}]\lambda 5007/\text{H}\beta$ - $[\text{O I}]\lambda 6300/\text{H}\alpha$ line ratio is more sensitive, and therefore a more reliable tracer, to changes in the ionization conditions due to fast shocks than any of the other optical emission line ratios involving $[\text{N II}]\lambda 6584/\text{H}\alpha$ or $[\text{S II}]\lambda 6725/\text{H}\alpha$ ratios (Dopita & Sutherland 1995). In the following subsections a more detailed discussion of the two-dimensional ionization structure of the ionized gas distribution based on the $[\text{O III}]\lambda 5007/\text{H}\beta$ - $[\text{O I}]\lambda 6300/\text{H}\alpha$ diagram and on the $[\text{O III}]\lambda 5007/\text{H}\beta$, and $[\text{O I}]\lambda 6300/\text{H}\alpha$ maps for the interface, IC 694, and NGC 3690 is given.

6.1. Interface region: Evidence for an off-nuclear Seyfert-like ionization cone

The $[\text{O III}]\lambda 5007/\text{H}\beta$ - $[\text{O I}]\lambda 6300/\text{H}\alpha$ line ratios have been obtained for all the INTEGRAL/SB3 individual spectra (Fig. 10). Although these data include the high surface brightness nuclear regions of IC 694 and NGC 3690, and their external regions, they also cover the area that has been identified as the interface zone, i.e. the extended low surface brightness region connecting the two galaxies up to distances of about 4 kpc from their nuclei. Changes in the ionization structure traced by the $[\text{O III}]\lambda 5007/\text{H}\beta$ and $[\text{O I}]\lambda 6300/\text{H}\alpha$ two dimensional spatial distribution line ratios are also shown (Fig. 10).

Three different types of ionization, H II-, LINER- and Seyfert-like, are identified, and the line ratio maps clearly show that the ionization structure has a well defined spatial distribution. The majority of the regions associated with the two individual galaxies (marked with two isocontours in the figure) are dominated by H II-like ionization, as expected from the intense star formation taking place there (see more details in §9). There are some exceptions; the nucleus B1 shows LINER-like activity at this angular resolution. The Seyfert-like ionization is clearly resolved with a size of about $7''$ (~ 1.5 kpc) and has a conical morphology, with an opening angle of about 54° and its apex located in nucleus B1 (at a projected distance of about 1.5 kpc from the peak of the nebula) within the angular resolution (see Fig.10). Moreover, this highly ionized gas is not associated to any particular concentration of stellar mass according to the optical (WFPC2/F814W; see Fig. 1) HST continuum image. Off-nuclear Seyfert-like nebulae at distances of few kpc from the nucleus have already been reported in other (U)LIRGs with Seyfert nucleus (Mrk 273: Colina et al. 1999), and interpreted as photoionization of extranuclear interstellar gas by the AGN. Therefore, our data strongly suggest photoionization by a radiation cone escaping from a central dust-enshrouded AGN source located in B1. The highly ionized conical structure in Arp 299 (NGC 3690) is also detected at distances of up to 4 kpc from B1; however, the ionization associated to these outer regions of the cone is LINER-like rather than Seyfert (Fig. 10). Therefore, it seems that within the cone there are two ionization regimes well separated spatially. At projected distances from B1 smaller than about 2 kpc the ionization is likely due to radiation coming from

the AGN located in B1, while at larger distances LINER-like ionization is dominant. This LINER-like ionization is also found in other areas of the interface region, however with a lower degree of excitation, as traced by the $[\text{O I}]\lambda 6300/\text{H}\alpha$ ratio measured in these regions.

6.2. IC 694

Over the area covered by the INTEGRAL SB2 bundle, H II and LINER-like ionization are present in this galaxy (Fig. 11). The main body of the galaxy, including the regions close to the nucleus A and the spiral arm structure (A7, G) towards the east (F), is dominated by the star-forming knots. LINER-like ionization is present elsewhere, being more prominent in diffuse low surface brightness regions located at a projected distance of about 1.8 kpc. The $[\text{N II}]\lambda 6584/\text{H}\alpha$ and the $[\text{S II}]\lambda 6725/\text{H}\alpha$ line ratio maps (not shown) also have a similar structure though, as explained above, they tend to indicate a lower ionization.

6.3. NGC 3690

Three types of excitation level (H II-, LINER- and Seyfert-like) are present in this individual galaxy, as shown in the $[\text{O III}]\lambda 5007/\text{H}\beta$ - $[\text{O I}]\lambda 6300/\text{H}\alpha$ diagnostic diagram and in the two dimensional maps (Fig. 12). Regarding the nucleus B1, these higher resolution data give a clear Seyfert-like classification in all these line ratios (Fig. 9), and show that there is an extended zone of about $2''$ (0.4 kpc) in length associated to B1 with Seyfert characteristic. This is the inner section of the AGN-like ionization cone detected with the SB3 bundle, with its apex coincident with B1. Moreover, the region B2 presents also a high ionization state in the border line of Seyfert/LINER, characteristic that could indicate the presence of the counter ionization cone. The detection of Seyfert-like activity based on optical emission lines represent the first evidence in the optical for the presence of an AGN in B1, and supports the recent claim of an AGN based on X-ray (Della Ceca et al. 2002) and mid-IR (Gallais et al. 2004) data. Previous spectroscopic studies in the optical (Gehrz et al. 1983; Coziol et al. 1998; Keel 1984) did not find AGN emission, probably due to the large size of the slits ($3''.6$, $2''.5$, and $8''.0$). This is in agreement with our results, where the Seyfert nature of the B1 nucleus has been diluted in the SB3 ($\phi = 2''.7$) spectra, whereas in the higher spatial resolution SB2 ($\phi = 0''.9$) spectra the classification is clear.

H II-like ionization dominates the rest of the main body of the galaxy (e.g. complex C), while LINER-like is present in a few outer regions. The $[\text{O I}]\lambda 6300/\text{H}\alpha$ map has its peak displaced about $0''.7$ (0.14 kpc) to the north with respect to B1. Similar displacements are observed in the $[\text{N II}]\lambda 6584/\text{H}\alpha$ and in the $[\text{S II}]\lambda 6725/\text{H}\alpha$ maps. These lines and in particular $[\text{O I}]\lambda 6300/\text{H}\alpha$ are a good tracers of shocks, thus these shifts may indicate different ionization mechanisms around B1 on scales of 200 pc. These small scale ionization changes need further investigation with high angular resolution spectroscopy.

7. ELECTRON DENSITY

The two-dimensional electron density maps of the ionized gas distribution have been derived for the entire Arp 299 system using the standard $[\text{S II}]\lambda 6716/[\text{S II}]\lambda 6731$ lines ratio (Aller 1984; Osterbrock 1989). The average

line ratio for the interface and the individual galaxies show a similar value, about 1.3 ± 0.1 , indicating an average uniform electron density ($\sim 100 \text{ cm}^{-3}$) over the entire Arp 299 system. However, the ionization cone detected in NGC 3690 presents a well defined gradient of this line ratio value, that roughly ranges from 1.2 ± 0.15 in the higher excitation (i.e. Seyfert-like) center of the cone, to 1.8 ± 0.15 in the lower excitation (i.e. LINER-like) outer section. Thus, the electron density seems to decrease from about 180 cm^{-3} at a distance of 1.5 kpc from B1 to less than 10 cm^{-3} at about 4 kpc.

8. THE ORIGIN OF THE LINER-LIKE IONIZATION

Most regions of the Arp 299 system have been classified as LINER-like, although the mechanism producing this ionization needs to be determined. Some authors have found in (U)LIRGs a positive correlation between the $[\text{O I}]\lambda 6300/\text{H}\alpha$ ratio and the velocity dispersion (Monreal-Ibero et al. 2006), which has been considered as evidence supporting the shocks as the origin for the ionization (Armus et al. 1989; Dopita & Sutherland 1995). The $[\text{O I}]\lambda 6300/\text{H}\alpha$ versus the $\text{H}\alpha$ velocity dispersion for all the spectra obtained with INTEGRAL has been represented (Fig. 13) in order to investigate the origin of the LINER-like ionization in Arp 299. The four main regions of the system observed with the INTEGRAL SB2 and SB3 bundles are analyzed separately: the inner and outer sections of the ionization cone, the interface region and finally the individual galaxies. The outer section of the ionization cone (stars in Fig. 13, *Left panel*). LINER-like excitation, i.e. $[\text{O I}]\lambda 6300/\text{H}\alpha > -1.25$ is independent of the velocity dispersion and present a stable ionization level, while with a wider variety in the ionization level, the inner section of the cone (Seyfert-like, triangles in Fig. 13, *left panel*) does not follow the correlation founded in external regions of ULIRGs (Monreal-Ibero et al. 2006). The interface region (crosses in Fig. 13, *Left panel*) present a stable LINER-like excitation level, and is not dependent of the velocity dispersion.

With regards to the individual galaxies IC 694 and NGC 3690 as observed with the lower angular resolution (SB3) bundle (filled circles in Fig. 13, *Left panel*), the ionization is mainly H II-like, with no evidence of a kinematical correlation. For the higher angular resolution (SB2) data (see Fig. 13, *Center and Right panels*), the actual measurements of the individual galaxies do not follow the correlation, although they present a well defined clustering. The galaxy IC 694 has a mean $\log \sigma \sim 1.8$, and presents about the same fraction of H II and LINER activity. In the case of NGC 3690 the velocity dispersion is clustered around $\log \sigma \sim 2$, and there is a large fraction of regions with H II-like ionization.

Clearly the present data show a different behavior than that found in ULIRGs (Monreal-Ibero et al. 2006), and this is probably due to the fact that on each case the measurements are done over regions located at different distances to the nucleus, and with different characteristics. The original correlation was derived for diffuse extra-nuclear regions in ULIRGs, which are located at distances of about 5–15 kpc from the nucleus of the galaxy. In the present case the interface region and the ionization cone have regions at distances of up to 4 kpc from the nucleus, and comparing with the original lim-

its of the correlation (see shaded area on Fig. 13, *Left panel*) the data of the interface and both regions of the ionization cone lie in general above the ratio, i.e. this regions show higher excitation for the same velocity dispersion. In the case of the individual galaxies observed with the actual higher resolution bundle (Fig. 13, *Center and Right panels*) the present data are closer to the nucleus than in the case of ULIRGs (up to ~ 2.5 kpc) and in most cases the regions involved are compact bright sources rather than diffuse. Comparing with the original limits of the relation (see shaded area on Fig. 13, *Center and Right panels*) the IC 694 data are clustered around, while the ones of NGC 3690 are below the correlation. This means that in the present case for the individual galaxies the star formation influence is still present, and that the velocity dispersion close to the nucleus traces mass rather than flows/shocks.

Given an ionization mechanism, the ionization state of the surrounding gas can be changed as a result of the variations in the electron density, that affect to the ionization parameter ($U \propto N_e^{-1} r^{-2}$). This appears to be the case in the outer high excitation cone associated to NGC 3690. As already mentioned, the electron density seems to have a radial variation within the cone, and by having the exact variation of N_e with r , the radial dependence of the parameter U would be described more precisely. Unfortunately in the present case the exact radial dependence of N_e cannot be derived; in spite of that, the variation detected on the electron density, and therefore the LINER activity could be accounted for by the influence of an AGN (if $N_e \propto r^{-\alpha}$). The variation of N_e implies a variation on the ionization parameter ($U \propto r^{-2+\alpha}$), and thus the low excitation is valid if the source is not local.

In conclusion, for the Arp 299 system studied here there are no clear evidences for tidally induced shocks as found in ULIRGs. Therefore, the origin for the LINER ionization is unclear, and at least in some zones (i.e. outer parts of the cone) it could, perhaps, be due to a radiation field similar to that of a low-luminosity AGN.

9. STAR FORMATION PROPERTIES

It is well known that merging processes between gas rich galaxies can trigger star formation. As predicted by numerical simulations (Mihos & Hernquist 1994), the process can vary depending on whether or not the parent disk galaxies have a bulge. The star-forming process at a low level ($\text{SFR} \sim 20 \text{ M}_\odot \text{ yr}^{-1}$) consequence of the merging of two disk galaxies without a bulge is produced early on in the merging phase, and can be sustained for about 150 Myr. On the other hand, in the merger of galaxies with a bulge the starburst ($\text{SFR} \sim 50\text{--}100 \text{ M}_\odot \text{ yr}^{-1}$) is produced later in the merging phase, and lasts for about 50 Myr.

To investigate the properties of the young stellar populations of a galaxy assuming instantaneous and continuous bursts, synthetic models such as SB99 (Leitherer et al. 1999; Vazquez & Leitherer 2005) can be used. In the following the stellar population synthesis model considers a Salpeter initial mass function (IMF), with lower and upper mass limits of 0.1 M_\odot and 100 M_\odot , the Geneva tracks with high mass loss, and the Calzetti extinction law (Calzetti et al. 2000). Instantaneous bursts are normalized to 10^6 M_\odot , while the continuous star formation is

normalized to a star formation rate of $1 \text{ M}_\odot \text{ yr}^{-1}$. Combining the information from the two dimensional distribution of the $\text{H}\alpha$ equivalent width and luminosity, and the photometric results, parameters such as the extinction to the gas, the age of the burst, and the stellar mass for each individual region can be derived. For the present analysis we use the INTEGRAL SB2 bundle with a resolution of $0''.9$ (i.e. 0.18 kpc), thus in the majority of cases the data include both the contribution from the stellar clusters and from a diffuse component.

9.1. Photometry of the regions of IC 694 and NGC 3690

The aperture photometry as derived by AAH00, using the HST NIC1 F110M, NIC2 F160W, NIC2 F222M images is used in the following analysis. In addition optical (WFPC2/F814W) photometry over the same regions, using the same apertures, and after performing the background subtraction and the aperture correction (for the latter see Holtzman et al. 1995) has been obtained. The apertures used were $0''.9$ diameter for the nuclei of IC 694 and NGC 3690 A and B1, and for the star-forming region B2, and $0''.5$ diameter for the rest of the star-forming regions. The HST magnitudes and colors derived are shown in Table 5. In addition, the HST magnitudes and colors were modeled by convolving the simulated galaxy spectral energy distribution with the system (optics, filter and detector) transmission function.

9.2. Properties of the $\text{H}\alpha$ emitting regions

In the following, instantaneous bursts models characterized by the predicted $\text{H}\alpha$ luminosity and equivalent width, and near-IR colors will be used to study the stellar populations of the $\text{H}\alpha$ emitting regions under analysis. Comparing the measured values with the models, it is possible to derive the age, extinction and mass of the individual regions under study. Regarding to the nucleus B1, and as previously indicated, it is classified as Seyfert, and the fraction of the ionizing flux coming from the buried AGN in this region is not well determined. Therefore the conclusions regarding the star formation properties in B1 based on the $\text{H}\alpha$ luminosity have to be taken with caution, and represent an upper limit. Because of this fact, the nucleus B1 is basically not included in the following discussion, although the properties derived are listed in the tables.

The $\text{H}\alpha$ luminosity in specific regions with large $\text{H}\alpha$ equivalent width (Fig. 14) traces preferentially the presence of young stellar populations ($<5\text{--}10 \text{ Myr}$). However, the presence of an old underlying population tends to decrease the EW, and therefore to underestimate the age of the young stellar population. In the case of IC 694 and NGC 3690 the respective nuclei A and B1, and the NGC 3690 brightest optical region B2 present low $\text{EW}(\text{H}\alpha)$. The ages derived from the $\text{EW}(\text{H}\alpha)$ for several individual regions are shown in Table 6.

With an age for the nucleus (A) of 5.3×10^6 years, IC 694 does not show a wide spread in age for the individual star-forming regions; almost all are around 5×10^6 years, except for I1 with 5.9×10^6 years and the youngest regions, concentrated towards the east of the spiral-like arm (F and G, with 3.3 and 3.4×10^6 years respectively). The galaxy NGC 3690 shows an average age for the individual regions of $\sim 5.5 \times 10^6$ years, with the eldest one (7.2×10^6 years) located towards the north of B2. The

youngest sources are located in the northern part of the galaxy, and correspond to complex C. Independent estimates (Satyapal et al. 1999) also based on instantaneous bursts and characterized by a Salpeter IMF, derived ages of about 6×10^6 years for the main components of the Arp 299 system, that are compatible with the results obtained here. Compared to AAH00, who used a different model with Gaussian bursts, the present age for B2 is younger, but applying their $\text{EW}(\text{Br}\gamma) \leq 5 \text{ \AA}$ to our model, the age for B2 is $\geq 7 \times 10^6$ years, compatible with the actual calculations.

Extinction and dust properties of the star-forming regions can be studied using the near-IR colors F110M-F160W (approximately $J\text{--}H$) and F160W-F222M (approximately $H\text{--}K$) together with the $\text{EW}(\text{H}\alpha)$. Under the assumption that the extinction to the stars is equivalent to the extinction towards the gas, the $\text{EW}(\text{H}\alpha)$ value is independent of A_V (Fig 15). We have unreddened both observed colors using a foreground screen model and the extinction derived from the $\text{H}\alpha/\text{H}\beta$ ratio, and compared with the models. Once corrected for extinction, and taking into account the error bars, in the majority of the regions the values are close to the predicted $A_V=2\text{--}3$ mag track. Thus in general the extinction derived from the $\text{H}\alpha/\text{H}\beta$ ratio presented in Tables 2 and 3 show an offset with respect to the ones predicted by the colors. There are two possible explanations for this discrepancy; on the one hand the extinction derived from the $\text{H}\alpha/\text{H}\beta$ ratio can be underestimated (see §5.4), on the other hand the discrepancy traces the contribution of hot dust emission. For the highly reddened regions (e.g. A, B1¹⁰, C1) the colors measured (and corrected by extinction) are very red. As already mentioned (and discussed by AAH00) one of the most plausible explanations for this color excess is the presence of hot dust ($T > 600 \text{ K}$), which would mainly affect the F160W-F222M color. In an attempt to take into account the contribution of the hot dust emission, the $\lambda^{-2} \cdot B_\lambda$ wavelength modified black-body thermal emission (Hildebrand 1983) has been used. The results demonstrate that depending on the temperature (which has not necessary to be homogeneous over the line of sight) and the amount of dust, the contribution of hot dust ($\sim 800 \text{ K}$) emission could represent, on average, about 80% of the K-band emission (Fig. 15, *Right panel*) for the highly extincted regions (A, B1, C1), and about 30% for the rest of the regions. This result supports our previous conclusion that the dust is more concentrated towards the nuclei and some particular regions, than in the extra-nuclear star forming regions.

An alternative to the presence of a hot dust emission is that the structure of the dust-gas distribution does not follow the simple screen geometry, but it is closer to a clumpy foreground or a mixed dust-star distribution. Assuming a model where the gas is homogeneously mixed with the stars, the effect of an $A_V=6$ mag over the F160W-F222M and F110M-F160W measured colors will produce bluer colors: about 0.3 and 0.4 mag respectively (Scoville et al. 2000; see Fig. 15). For the extreme case $A_V=30$, the corresponding shifts will be 0.6 and 0.8 mag, i.e. in region C1 the F160W-F222M color will move from

¹⁰ In this discussion related to the hot dust the nucleus B1 is included, because even with high errors in the age derived from the $\text{EW}(\text{H}\alpha)$, the color excess exists and needs to be explained.

the observed 2.67 to 2.07. Thus the colors modeled with this alternative dust geometry would imply that a hot dust contribution is not mandatory in the external less extincted regions, but it is still required to explain the color excess, in the highly extincted regions (A, B1 and C1).

The stellar mass of the young population has been measured using two different indicators, the $H\alpha$ luminosity and the M_{160W} absolute magnitude, and comparing with the predicted values for the ages derived using the $EW(H\alpha)$. In both cases the $H\alpha/H\beta$ ratio has been used for correct by extinction (for A and C' the $Pa\alpha/H\alpha$ ratio was used too).

The results obtained using M_{160W} (see Fig. 16 and Table 6) show that the regions with more young stellar mass content are nucleus A and regions B2, B21 and C1 ($460, 300, 58$ and $81 \times 10^6 M_{\odot}$ respectively). The stellar mass content for the rest of the regions, including the low-surface brightness knots, ranges between 3.1 and $14.0 \times 10^6 M_{\odot}$ (details on Table 6). Previous derivations of the stellar mass of the clusters using absolute H-band magnitudes vs H-K (not corrected for extinction) with a different stellar populations synthesis model range, from about $1.5 \times 10^5 M_{\odot}$ to $5.0 \times 10^6 M_{\odot}$ (AAH00).

Using the $H\alpha$ luminosity, the young stellar mass content is again concentrated on the nucleus A, and regions B2, B21 and C1 ($655, 679, 74$ and $74 \times 10^6 M_{\odot}$ respectively). For region C', where there is not near-IR photometry, the mass derived using the $H\alpha$ luminosity is $115 \times 10^6 M_{\odot}$. The rest of the derived masses range from 5.7 to $57 \times 10^6 M_{\odot}$. Comparing the mass in newly formed stars with the derivations of AAH00, there are no significant differences except for B2 where we derive a value two times higher. The masses of the young $H\alpha$ -emitting regions identified in Arp 299 are within the range of masses founded in LIRGs (3×10^6 - $10^8 M_{\odot}$, Scoville et al. 2000; Alonso-Herrero et al. 2002) and are on average about 100 times more massive than the galactic globular clusters ($10^5 M_{\odot}$, van den Bergh 1995), probably due to the fact that the present regions have conglomerates of less massive clusters.

When comparing the stellar masses derived with the $H\alpha$ luminosity with the mass obtained from the absolute F160W magnitude, there is a good agreement in the nucleus A, but for the rest of the regions there are differences from a factor ~ 1 to 5. One of the main reasons for this difference is that in the majority of the cases (except A and B2) an aperture of $0''.5$ has been used for the HST cluster photometry, instead the $0''.9$ or $1''.0$ used for the INTEGRAL data analysis (for the $EW(H\alpha)$ and $L(H\alpha)$ estimates); this difference can lead to offsets of a factor 3 in the mass estimates. Factoring in the aperture effects, the two methods give the same mean value within a factor 2.

9.3. Contribution to the bolometric luminosity

The derived ages of the young $H\alpha$ -emitting star-forming regions cover a range of between 3×10^6 years to at least 7 - 8×10^6 years old. This is consistent with the methodology used here: since the $H\alpha$ traces preferentially the massive young ionizing stellar clusters, population older than 10 Myr is difficult to be detected as $H\alpha$ decreases. In any case there is further evidence that the star formation in Arp 299 has persisted for at least

the last 10 - 15×10^6 years (AAH00), with high activity on the star-forming regions. On the basis of this dispersion, we consider that the overall star formation of Arp 299 can be modeled by a continuous star formation. Under this premise the star formation rate (SFR) and the IR luminosity contribution can be derived from the extinction corrected $H\alpha$ luminosity, using Kennicutt (1998) expressions, valid for a Salpeter IMF with mass cutoffs of 0.1 - $100 M_{\odot}$:

$$SFR(M_{\odot} \text{ year}^{-1}) = 7.9 \times 10^{-42} L(H\alpha) (\text{erg s}^{-1}) \quad (1)$$

$$L_{IR} (\text{erg s}^{-1}) = 175.5 \times L(H\alpha) (\text{erg s}^{-1}) \quad (2)$$

that strictly speaking are only valid for starbursts with ages less than 10^8 years.

Without taking into account the nucleus B1 (AGN candidate), the SFR of the entire system is about $43 M_{\odot} \text{ year}^{-1}$, and the L_{IR} is $9.5 \times 10^{44} \text{ erg s}^{-1}$, whereas the luminosity derived from the IRAS fluxes is $2.2 \times 10^{45} \text{ erg s}^{-1}$, thus the contribution of the studied regions to the IR luminosity is about 45%. There is a lack of about 55% in luminosity, that can be accounted for by the AGN located in B1. Previous estimates based on the mid and far-IR spectra of Arp 299 assign a 20% of the L_{IR} coming from B1 and B2 (Charmandaris et al. 2002), while at $11.7 \mu\text{m}$ the percentage of flux coming from B1 and B2 is about 30% (Keto et al. 1997). So even considering that the majority of this contribution comes from B1, there is still a lack of about 25–35%. This inconsistency is probably due to the fact that the present result is limited by the derived extinction and/or the models.

10. 2D GAS KINEMATICS AND DYNAMICAL MASS DERIVATIONS

Previous studies of Arp 299 (Gehrz et al. 1983; Telescope et al. 1985) concluded that this system consists of two spiral galaxies disturbed by the merging process, which are rotating in opposite sense (Augarde & Lequeux 1985). More recently Hibbard & Yun (1999) have described Arp 299 as a structure formed after a prograde-retrograde encounter between IC 694 (Sab-Sb) and NGC 3690 (Sbc-Sc) that took place some 750 Myr ago, and having a long tidal tail (180 kpc in length) detected in H I. Although there are still two structures clearly distinguishable with the two nuclei separated by about 4.6 kpc, the warm gas component has lost its kinematic identity and the velocity field presents a very irregular pattern (Rampazzo et al. 2005).

10.1. Gas kinematics

The kinematics of the ionized and the neutral gas is traced by the $H\alpha$ emission line and the $\text{Na I } \lambda 5890$ absorption line respectively (Sparks et al. 1997). The ionized gas mean velocities and velocity dispersions were obtained by fitting the $H\alpha + [\text{N II}] \lambda \lambda 6548, 6584$ complex with a single Gaussian velocity component per line; the same method was applied to the $\text{He I } \lambda 5876 + \text{Na I } \lambda \lambda 5890, 5896$ complex. The values derived for the individual regions are presented in Tables 7, 8 and 9. For the velocity measurements, the errors have been calculated taking into account both the systematic uncertainties of the wavelength calibration (same for all lines) in the velocity

measurement, and the uncertainties in the measurement of the centroid of the line (that depends on the S/N of the studied line). One of the most relevant results obtained is that the two dimensional structure of the ionized and neutral gas velocity field show similar features in both the individual galaxies and the interface region, indicating that the ionized and neutral gas kinematics are coupled.

The structure of the H α velocity dispersion shows that there is a variation on the average velocity dispersion values: the interface region has the lowest (45 km s $^{-1}$), IC 694 the intermediate (65 km s $^{-1}$) and NGC 3690 (120 km s $^{-1}$) the maximum values of σ .

10.1.1. Interface Region

The overall velocity field of the ionized gas as observed with the SB3 bundle has a complex and irregular pattern, that does not indicate the presence of virialized simple (e.g., rotating) motions, on scales of 0.6 kpc or larger (Fig. 17, *Left*). The structure of this map agrees well with that obtained by Rampazzo et al. (2005) covering a larger area (FoV of 5'.9) on the sky. The velocities in the northern part are receding, and in the southern part are approaching to the systemic value, defined as the velocity in nucleus A (the dust-enshrouded nucleus of IC 694) with the higher spatial resolution bundle SB2, $V_A = 3121 \pm 27$ km s $^{-1}$ (see section §10.1.2). The corresponding lower spatial resolution SB3 velocity is $V_A = 3190 \pm 27$ km s $^{-1}$.

The velocity field of the neutral gas obtained from the NaD absorption lines, despite of being noisier (the intensity of the NaD can be typically 2% of that of H α), shares similar structural characteristics with the ionized gas velocity field (Figure 17 *Center panel*), and presents a systemic velocity of 3057 ± 34 km s $^{-1}$.

The ionized gas velocity field presents a peak-to-peak velocity of about 230 km s $^{-1}$, while for the neutral gas the variation is smaller, about 170 km s $^{-1}$. In both cases the area with the largest approaching velocities is close to B2. The ionization cone does not show relevant features in the ionized gas velocity field, nor in the neutral gas velocity field. With the exception of the nuclear regions, the ionized gas in the galaxies does not have a distinct kinematics with respect to the interface region (i.e., the structure of the velocity field does not correlate with the distribution of mass as traced by the continuum images).

The velocity gradient of the ionized gas through the interface is about 40 km s $^{-1}$ kpc $^{-1}$, compatible with the H α velocity gradients previously measured across ULIRGs observed with a slit (up to 47 km s $^{-1}$ kpc $^{-1}$ for galaxies with double nuclei, Martin 2006).

The velocity dispersion shows distinct features over the entire area; there are large differences in σ , that allow us to discriminate spatially between quiet and turbulent gas with macroscopic motions (Fig. 17 *Right panel*). The so-called interface has an average σ value of 45 km s $^{-1}$ that traces no turbulent gas. The low velocity amplitude and velocity dispersion of the interface indicates that the ionized gas could be in a close to quiescent phase or slowly rotating. Larger σ values are measured on the previously defined ionization cone, with the maximum (160 ± 21 km s $^{-1}$) located on the peak of Seyfert-like ionization. This spatial coincidence could indicate that in that area the two contributions of the biconic surface of the cone are

added, and thus the line measured is wider (Heckman et al. 1990). On the other hand, the maximum velocity dispersion would imply that the largest macroscopic motions, with approaching velocities, are taking place in that highly ionized area.

10.1.2. IC 694

The velocity field of both the ionized and neutral gas presents a similar structure (Fig. 18 *Left and Center panels*), when observed with the SB2 bundle. It has an irregular structure, with the largest receding velocities associated with region I (3181 ± 27 km s $^{-1}$ for the ionized gas and 3155 ± 34 km s $^{-1}$ for the neutral), located at 0.42 kpc SW from the nucleus (A). These maps show a general trend with velocities changing from NW (receding) to SE (approaching), in agreement with the pattern found with the SB3 data in this region. The systemic velocity for the ionized gas is defined as the velocity associated with the nucleus (region A), and it has a value of 3121 ± 27 km s $^{-1}$, consistent with Zhao et al. (1997) estimate based on the H92 α radio recombination line (3120 ± 50 km s $^{-1}$). The ionized gas velocity field has a peak-to-peak variation of 290 km s $^{-1}$. The neutral gas systemic velocity is 3057 ± 34 km s $^{-1}$, and the peak-to-peak velocity is about 216 km s $^{-1}$. Although evident structural similarities are found between the ionized and neutral gas (i.e. same kinematics), in general the velocity of the neutral gas presents a blueshift over the entire area with respect to the ionized gas (about -30 ± 12 km s $^{-1}$ over the studied regions). This systematic blueshift appears to be real taking into account the uncertainties. In that case, this is a marginal effect, with a lower value than the ones measured in ULIRGs using a slit (Martin 2006; from about -60 km s $^{-1}$ to -300 km s $^{-1}$). In the present analysis the value obtained is derived from IFS data, i.e. has the advantage of the two dimensional distribution versus the use of the slit, where the measurements are limited to a restricted area, probably centered on the nuclear regions.

Across the galaxy there are gradients of about 110 km s $^{-1}$ kpc $^{-1}$ in the ionized gas velocity (between regions located ~ 2.3 kpc apart i.e. $\sim 11''$), higher than the typical values founded in ULIRGs (up to 60 km s $^{-1}$ kpc $^{-1}$ for an individual galaxy, Martin 2006) when using a slit of 20'' long. In closer regions with large velocity variations the gradients can be 150 km s $^{-1}$ kpc $^{-1}$ (between regions I and northern of G, located about 1.4 kpc apart). In spite of these gradients, and as discussed below, there are no clear evidence for virialized simple rotating motions.

The two-dimensional velocity dispersion map shows a different structure than the velocity field (Fig. 18, *Right panel*). For nucleus A, the σ value is 108 ± 11 km s $^{-1}$, in well agreement with the derivation of Shier et al. (1996) based on the CO(2,0) near-infrared band at 2.3 μ m (135 ± 21 km s $^{-1}$). The maximum value for σ (170 ± 20 km s $^{-1}$) is located in a region 0.28 kpc towards the north-east of A, where the [O I] λ 6300 emission peak is also located. Since [O I] λ 6300 trace shocks, this high σ value is a hint of turbulence and shocks. The lowest velocity dispersion (lower limit 25 ± 3 km s $^{-1}$) corresponds to the area dominated by H II-like ionization, towards the east of the spiral arm (e.g. A7, see §6.2). This indicates that the velocity dispersion is likely dominated by the internal kinematics within the stellar clusters, rather than

by large regions projected along the line of sight.

In this case it is not possible to state that there are clear indication of pure rotation, i.e. the photometric peak does not coincide with the velocity dispersion maximum, and neither of them coincide with the possible kinematic center. The velocity maps show that even if pure rotation does not dominate the galaxy kinematics, rotational movements can be present.

10.1.3. NGC 3690

Like in the previous case, at a resolution of 0.18 kpc the structure of the ionized and neutral gas velocity fields obtained with the SB2 bundle are very similar (Fig. 19 *Left and Center panels*). The largest receding velocities are detected towards the north-east of the field (C', C6), while the largest approaching velocities are located on B2 and towards the south-west. The ionized gas systemic velocity is defined as the one of the nucleus B1, with a value of $3040 \pm 27 \text{ km s}^{-1}$. This value coincides with Zhao et al. (1997) measurements using the H92 α radio recombination line ($3080 \pm 40 \text{ km s}^{-1}$). For the ionized gas, the peak-to-peak velocity is 257 km s^{-1} . The systemic velocity measured with the neutral gas is $2976 \pm 32 \text{ km s}^{-1}$, with a peak-to-peak variation of 217 km s^{-1} . In both ionized and neutral gas, the velocity variations are similar to the ones measured in IC 694. As founded in ULIRGs (Martin 2006), there is a systemic blueshift of the neutral gas velocity with respect to the ionized gas (about $-24 \pm 13 \text{ km s}^{-1}$ in the studied regions). Due to its value, lower than the results founded for ULIRGs (from about -60 km s^{-1} to -300 km s^{-1} , Martin 2006), this blueshift is consider as a marginal effect.

Across the galaxy there are gradients of about $70 \text{ km s}^{-1} \text{ kpc}^{-1}$ in the ionized gas (between C' and D3). This result is close to the gradients derived for ULIRGs using a slit (up to $60 \text{ km s}^{-1} \text{ kpc}^{-1}$ for an individual galaxy, Martin 2006).

The two-dimensional structure of the velocity dispersion ranges between 50 ± 5 and $172 \pm 20 \text{ km s}^{-1}$ (Fig. 19 *Right panel*), and present different characteristics than the two dimensional velocity fields. The nucleus B1 has the maximum velocity dispersion value of the entire system ($172 \pm 20 \text{ km s}^{-1}$), and regions with high velocity dispersion ($\sim 160 \text{ km s}^{-1}$) are also detected about 1 kpc towards the north and north-west of B1. Looking at the ionized gas velocity field, this secondary peaks of the velocity dispersion are located in regions where there are high velocity variations (from approaching to receding), and thus this σ would represent a convolution of a large velocity gradient. Although the σ -peak coincides spatially with the nucleus, and then it would be tracing the mass (large σ implies that this is the most massive galaxy of the system), the presence of an AGN in B1 could produce a broadening of the line width.

Like in the case of IC 694 there are no clear evidences for ordered rotating motions; the photometric and velocity dispersion peaks do not coincide with the possible kinematic center. In conclusion, although the pure rotation does not dominate the kinematics of the galaxy, rotational process would be present.

10.2. Where is the true nucleus of NGC 3690?

The galaxy NGC 3690, shows variations on the surface brightness importance of the regions B1 and B2 with

wavelength. While in the ultraviolet (Windhorst et al. 2002) and in the optical (this work) B2 appears brightest than B1, and therefore has been identified as the nucleus, the reverse is true in the near-IR ($2.2 \mu\text{m}$ AAH00) and mid-IR (Gallais et al. 2004). Besides, the optical kinematical analysis shows that the σ peak is located in B1 (see §10.1.3). This fact along with the high extinction ($A_V=3.7$), the hot dust component needed to explain the color excess, and the presence of an AGN, lead us to the conclusion that B1 is the true nucleus of the individual galaxy NGC 3690, as previously discussed by Gallais et al. (2004) with mid-IR spectro-imaging, and concluded by Zezas et al. (2003) using Chandra X-ray observations.

10.3. Dynamical mass derivation of the nuclei and brightest regions

Until now the only mass derivation in this work has been done for the H α -emitting young star forming regions. The central ionized gas velocity dispersion is a good tracer of the dynamical mass, thus it can be used as an alternative method for mass derivation. Assuming virialization, the dynamical mass of the nuclei and brightest regions can be derived as:

$$M_{\text{dyn}} = 1.75 \times 10^3 R_{\text{hm}} \sigma^2 M_{\odot} \quad (3)$$

where R_{hm} is the half mass radius in pc and σ is the velocity dispersion in km s^{-1} . Assuming a constant value of 1.75 (see Colina et al. 2005 for a detailed discussion), and that the effective radius (R_{eff}) of the light distribution traces the half mass radius in each region, it is possible to infer the total dynamical mass.

In the present treatment we assume that H α is traced by P α , that gives the real size of the emitting regions. In consequence the effective radius of the most important emitting sources is calculated over the HST P α image; additional estimates using the F110M image are done for comparison. There are some caveats related to the spatial resolution of the different set of data worth mentioning. For this mass estimate we are dealing with information at different spatial resolutions: on the one hand the velocity dispersion from the INTEGRAL SB2 bundle data was measured at a $0''.9$ ($\sim 180 \text{ pc}$) resolution. On the other hand the R_{eff} over the most relevant Arp 299 regions (i.e. the ones resolved) was measured using the NICMOS1/F110M image ($0''.043/\text{pix}$, i.e. $\sim 9 \text{ pc}/\text{pix}$) and NICMOS2/P α image ($0''.076/\text{pix}$, i.e. $\sim 16 \text{ pc}/\text{pix}$). The typical size of the H II regions in LIRGs is 200-300 pc (Alonso-Herrero et al. 2002), i.e. several times larger than the effective radius of the stellar clusters and about the size of a SB2 fiber. Taking this into account, the clusters will be point sources for INTEGRAL, and their σ will be integrated on the fiber.

For nucleus A we derive a dynamical mass of about $1.2 \times 10^9 M_{\odot}$ (Table 10) which is about 5 times smaller than the derivation done by Shier et al. (1996) using the velocity dispersion measured from the $2.3 \mu\text{m}$ CO band; this discrepancy is due to a different estimate of the radius ($r_{\text{CO}}/r_{\text{P}\alpha} \simeq 4$). The calculated M_{dyn} implies that the young stellar mass content derived from L(H α) in A is about 40%. The mean value for the dynamical mass of nucleus B1 is $1.5 \times 10^9 M_{\odot}$ (in good agreement with Shier et al. 1996), consequently the upper limit for the young

stellar mass content is about 15%. For B2 the mean value of the total mass is $0.6 \times 10^9 M_\odot$ (the same as Shier et al. 1996). This would imply that about 100% of the mass in B2 is from young stellar population, indicating that the mass derivation done using $L(H\alpha)$ is probably overestimated. For the last two regions (C1 and C'), the R_{eff} gives an upper limit for the dynamical mass (0.6 and $0.3 \times 10^9 M_\odot$ respectively, the latter according to the $>0.1 \times 10^9 M_\odot$ from AAH00), that implies young stellar mass contents of about 13% and 40% respectively.

11. SUMMARY

A detailed IFS study of the LIRG Arp 299 (IC 694+NGC 3690) system covering a region of 7.0×6.2 kpc has been presented. This work illustrates the flexibility and power of the IFS in studying in two dimensions and simultaneously the different physical properties, such as stellar populations, internal dust extinction, ionization structure and gas kinematics, of complex systems like Arp 299. In what follows only the main results of this study are summarized:

1. The observed overall two dimensional stellar and ionized gas structure differs due to internal extinction effects caused by the dust, and to the different spatial distribution of the diverse (AGN, stars, shocks) ionizing sources. The stellar continuum and emission line distribution peaks are not spatially coincident but separated up to 1.4 kpc. The peaks of the ionized gas traced by different emission lines (e.g. hydrogen recombination, high excitation [OIII], and shock-tracer [OI]) are also not coincident indicating that the ionizing mechanisms change on scales of about 200 pc or less.
2. The region B1 is identified as the true nucleus of NGC 3690. The presence of an AGN in B1 is inferred from the detection of a high-excitation Seyfert-like conical structure of about 1.5 kpc in size, an opening angle of about 54° , and its apex being located in B1. This region also presents the additional characteristics of a dust -enshrouded nucleus with high extinction ($A_V = 3.7 \pm 0.6$), red colors ($F160W-F222M = 2.06 \pm 0.1$) indicating hot dust emission, and high velocity dispersion ($\sigma = 172 \pm 20$ km s $^{-1}$).
3. The observed near-IR colors reveal the presence of hot dust over the entire structure. According to the $F160W-F222M$ color, the upper limit for the mean hot dust contribution is about 30% at 600 K for the majority of the star-forming regions. The nuclei A and B1, and region C1 are the most affected by the

hot dust component, with an upper limit of about 70%, 80% and 90% at 600 K respectively.

4. The high surface brightness regions are mainly dominated by star formation, while the low surface brightness regions are dominated by LINER-like ionization process. The $H\alpha$ -emitting star-forming regions present an extinction of between $A_V = 1-6$ mag, with ages between 3.3 and 7.2×10^6 years, and masses that range between about 6 and $680 \times 10^6 M_\odot$. The total contribution (extinction corrected) of these sources to the bolometric luminosity is about 45%.
5. The structure of the ionized ($H\alpha$) and neutral (NaD) gas two dimensional velocity fields show similar features, indicating that both components are kinematically coupled on scales of hundreds of pc and larger. The velocity fields are very complex, and in general the galaxy does not appear to be dominated by ordered virialized simple (e.g. rotation) motions. The morphology of the velocity field does not correlate with the distribution of mass as traced by the continuum images, that is, no spatial coincidence between the kinematic and the photometric centers exists.

On average, the interface region presents the lowest value of velocity dispersion ($\sigma \sim 45$ km s $^{-1}$), IC 694 presents the intermediate values ($\sigma \sim 65$ km s $^{-1}$), and NGC 3690 the highest ($\sigma \sim 120$ km s $^{-1}$). This indicate that NGC 3690 is the warmest body of the entire system, and probably the most massive. On the contrary, the low velocity amplitude and velocity dispersion of the interface suggests that the ionized gas is slowly rotating or in a close quiescent phase.

The velocity dispersion measurements over the nuclei and the brightest emitting regions, imply a mean value for the dynamical mass of about $1.2 \times 10^9 M_\odot$ and 1.5×10^9 for nuclei A and B1 respectively, within a mean radius of 58 pc and 28 pc. For regions B2, C1 and C' the mass ranges between $\sim 0.2 \times 10^9 M_\odot$ and $\sim 0.6 \times 10^9 M_\odot$, within a radius of about 30 pc.

Acknowledgments

The authors wish to thank Dr. Hajime Sugai, the referee, for his detailed and constructive report. We thank Jesús Maíz-Apellániz for his help using *jmaplot*. This work has been supported by the Spanish Ministerio de Educación y Ciencia, under grant BES-2003-0852, projects AYA2002-01055 & ESP2005-01480.

REFERENCES

- Aller, L. H. 1984, *Physics of Thermal Gaseous Nebulae* (Dordrecht:Reidel)
- Alonso-Herrero, A., Rieke, G. H., Rieke, M. J., Colina, L., Pérez-González, P. G., & Ryder, S. D 2006, *ApJ*, in press, astro-ph/0606186
- Alonso-Herrero, A., Rieke, G. H., Rieke, M. J., & Scoville, N. Z., 2002, *AJ*, 124, 166
- Alonso-Herrero, A., Rieke, G. H., Rieke, M. J., & Scoville, N. Z. 2000, *ApJ*, 532, 845
- Armus, L., Heckman, T. M., & Miley, G. K. 1989, *ApJ*, 347, 727
- Arribas, S. et al. 1998, *Proc. SPIE*, 3355, 821
- Arribas, S., Mediavilla, E., García-Lorenzo, B., & del Burgo, C. 1997, *ApJ*, 490, 227
- Augarde, R., & Lequeux, J. 1985, *A&A*, 147, 273
- Baan, W. A., & Haschick, A. 1990, *ApJ*, 364, 65
- Baldwin, J. A., Phillips, M. M., & Terlevich, R. 1981, *PASP*, 93, 5
- Ballo, L., Braitto, V., Della Ceca, R., Maraschi, L., Tavecchio, F., & Dadina, M. 2004, *ApJ*, 600, 634
- Bingham, R. G., Gellatly, D. W., Jenkins, C. R., & Worswick, S. P. 1994, *Proc. SPIE*, 2198, 56
- Calzetti, D. et al. 2005, *ApJ*, 633, 871

- Calzetti, D., Armus, L., Bohlin, R. C., Kinney, A. L., Koornneef, J., & Storchi-Bergmann, T. 2000, *ApJ*, 533, 682
- Charmandaris, V., Stacey, G. J., & Gull, G. 2002, *ApJ*, 571, 282
- Colina, L., Arribas, S., & Monreal-Ibero, A. 2005, *ApJ*, 621, 725
- Colina, L., Arribas, S., & Borne, K. D. 1999, *ApJ*, 527, L13
- Coziol, R., Torres, C. A. O., Quast, G. R., Contini, T., & Davoust, E. 1998, *ApJS*, 119, 239
- Della Ceca, R. et al. 2002, *ApJ*, 581, 9
- Dopita, M. A., & Sutherland, R. S. 1995, *ApJ*, 455, 468
- Gallais, P., Charmandaris, V., Le Floch, E., Mirabel, I. F., Sauvage, M., Vigroux L., & Laurent O. 2004, *A&A*, 414, 845
- García-Lorenzo, B., Acosta-Pulido, J. A., & Megias-Fernández, E. 2002, *ASPC*, 282, 501
- Gehrz, R. D., Sramek, R. A., & Weedman, D. W. 1983, 267, 551
- Heckman, T. M., Armus, L. & Miley, G. K. 1990, *ApJS*, 74, 833
- Hibbard, J. E., & Yun, M. S. 1999, *AJ*, 118, 162
- Hildebrand, R. H. 1983, *QJRAS*, 24, 267
- Holtzman, J. A., et al. 1995, *PASP*, 107, 156
- Howarth, I. D., & Murray, J. 1988, *DIPSO A Friendly Spectrum Analysis Program* (Starlink User Note 50; Chilton: Rutherford Appleton Lab.)
- Keel, W. C. 1984, *ApJ*, 282, 75
- Kennicutt, R. C. 1998, *ARA&A*, 36, 189
- Keto, E. et al. 1997, *ApJ*, 485, 598
- Laurent, O., Mirabel, I. F., Charmandaris, V., Gallais, P., Madden, S. C., Sauvage, M., Vigroux, L., & Cesarsky, C. 2000, *A&A*, 359, 887
- Leitherer, C., et al. T. M. 1999, *ApJS*, 123, 3
- McLeod, B. 1997, in *Proc. STScI Symp., The HST Calibration Workshop*, ed. S. Casertano, R. Jederzejewski, C. D. Keyes, & M. Stevens (Baltimore: STScI), 281
- Mannucci, F., et al. 2003, *A&A*, 401, 519
- Martin, C. L. 2006, *astro-ph* 0604173
- Mattila, S. et al. 2005, *IAUC*, 8473, 1
- Mihos, J. C., & Hernquist, L. 1994, *ApJ*, 431, L9
- Moshir, M., et al. 1993, *VizieR On-line Data Catalog: II/156A*
- Monreal-Ibero, A., Arribas, S., & Colina, L. 2006, *ApJ*, 637, 138
- Neff, S. G., Ulvestad, J. S., & Teng, S. H. 2004, *ApJ*, 611, 186
- Origlia L., & Leitherer C. 2000, *AJ*, 119, 2018
- Osterbrock, D. E. 1989, “Book-Review - Astrophysics of Gaseous Nebulae and Active Galactic Nuclei” (University Science Books)
- Rampazzo, R., Plana, H., Amram, P., Bagarotto, S., Boulesteix, J., & Rosado, M. 2005, *MNRAS*, 356, 1177
- Sanders, D. B., & Mirabel, I. F. 1996, *ARA&A*, 34, 749
- Satyapal, S., Watson, D. M., Pipher, J. L., Forrest, W. J., Fischer, J., Greenhouse, M. A., Smith, H. A., & Woodward, C. E. 1999, *ApJ*, 516, 704
- Savage, B. D., & Mathis, J. S. 1979, *ARA&A*, 17, 73
- Scoville, N. Z., et al. 2000, *AJ*, 119, 991
- Shier, L. M., Rieke, M. J., & Rieke, G. H. 1996, *ApJ*, 470, 222
- Sparks, W. B., Carollo, C. M., & Macchetto, F. 1997, *ApJ*, 486, 253
- Stanford, S. A., & Wood, D. O. S. 1989, *ApJ*, 346, 712
- Sugai, H., Davies, R. I., Malkan, M. A., McLean, I. S., Usuda, T., & Ward, M. J. 1999, *ApJ*, 527, 778
- Telesco, C. M., Decher, R., & Gatley, I. 1985, *ApJ*, 299, 896
- van den Bergh, S. 1995, *Nature*, 74, 215
- Vazquez, G. A. & Leitherer, C. 2005, *ApJ*, 621, 695
- Veilleux, S., & Osterbrock, D. E. 1987, *ApJS*, 63, 295
- Windhorst, R. A. et al. 2002, *ApJS*, 143, 113
- Zezas, A., Ward, M. J., & Murray, S. S. 2003, *ApJ*, 594, L31
- Zhao, J., Anantharamaiah, K. R., Goss, W. M., & Viallefond, F. 1997, *ApJ*, 482, 186

TABLE 1
PROPERTIES OF THE REGIONS OF THE IC 694+NGC 3690 INTERFACE

Reg	Dist ^a (kpc)	$\Delta\alpha^a$ (arcsec)	$\Delta\delta^a$ (arcsec)	$F_{obs}(\text{H}\alpha)^b$	A_V^c (mag)	$\log([\text{OIII}]/\text{H}\beta)^d$	$\log([\text{OI}]/\text{H}\alpha)^e$	$\log([\text{NII}]/\text{H}\alpha)^f$	$\log([\text{SII}]/\text{H}\alpha)^g$
K1	2.97	-17.6	-12.7	1.7	2.2	0.27	-1.07	-0.34	-0.37
K2	3.81	-21.6	-13.7	1.1	0.9	0.07	-1.04	-0.36	-0.38
K3	1.28	-9.6	-10.7	0.6	2.0	0.22	-0.59	-0.21	-0.25
K4	2.49	-13.0	-1.8	2.7	1.6	0.04	-0.83	-0.41	-0.31
K5	3.53	-14.5	3.9	10.7	2.9	0.14	-1.44	-0.54	-0.64
K6	3.71	-13.1	6.0	5.7	2.3	-0.05	-1.27	-0.48	-0.54
K7	2.72	-10.6	1.9	4.0	2.0	0.01	-1.10	-0.47	-0.45
K8	4.07	-9.0	9.8	1.4	2.7	0.14	-0.71	-0.32	-0.23
K9	3.52	-2.6	7.8	3.3	1.8	-0.01	-0.92	-0.37	-0.36
K10	5.26	-21.5	-9.0	4.2	1.0	0.17	-1.36	-0.53	-0.56
K11	1.44	-9.1	-5.1	1.6	1.5	0.02	-0.82	-0.39	-0.31
K12	3.18	-16.8	-17.4	7.6	2.0	0.13	-0.98	-0.35	-0.37

NOTE. — (a): Distance relative to the nucleus A. (b): Flux measured ($\times 10^{-14} \text{erg s}^{-1} \text{cm}^{-2}$) using a circular aperture of $3''$. Uncertainties 10%-15%. (c): Internal extinction derived from the $\text{H}\alpha/\text{H}\beta$ ratio. Average error in A_V is 0.7 magnitudes. (d): Average error ± 0.11 (e): Average error ± 0.06 (f): Average error ± 0.05 (g): Average error ± 0.06 . In all cases, emission line ratios are derived using extinction corrected flux values.

TABLE 2
PROPERTIES OF THE REGIONS OF IC 694

Reg	Dist ^a (kpc)	$\Delta\alpha^a$ (arcsec)	$\Delta\delta^a$ (arcsec)	$F_{obs}(H\alpha)^b$	A_V^c (mag)	$\log([OIII]/H\beta)^d$	$\log([OI]/H\alpha)^e$	$\log([NII]/H\alpha)^f$	$\log([SII]/H\alpha)^g$
A	0.00	0.0	0.0	2.9	2.9	-0.14	-1.03	-0.31	-0.41
A1	0.46	1.5	-1.6	2.6	2.3	-0.22	-1.29	-0.40	-0.50
A2	0.54	-1.0	-2.4	3.1	2.0	-0.14	-1.51	-0.52	-0.60
A3	1.37	3.3	-5.7	2.3	1.9	-0.03	-1.61	-0.53	-0.59
A4	1.51	3.8	-6.3	3.0	2.1	-0.02	-1.73	-0.55	-0.66
A5	1.06	-2.1	-4.7	6.0	1.9	0.10	-1.56	-0.54	-0.62
A6	1.00	-3.6	-3.9	4.0	2.1	0.04	-1.46	-0.52	-0.56
A7	0.99	-2.8	-3.9	6.2	2.3	0.09	-1.61	-0.56	-0.66
F	1.58	6.5	-4.1	6.7	3.2	0.10	-2.06	-0.52	-0.92
G	1.10	1.1	-5.2	6.2	1.9	0.05	-1.84	-0.54	-0.74
H1	0.48	2.3	-0.3	6.4	2.8	-0.15	-1.41	-0.47	-0.63
H2	0.34	1.6	0.5	4.7	3.4	-0.06	-0.99	-0.32	-0.46
I	0.42	-1.8	-0.9	6.0	1.6	-0.09	-1.60	-0.52	-0.65
I1	1.45	-7.0	0.8	0.8	2.4	-0.10	-1.28	-0.43	-0.42

NOTE. — (a): Distance relative to the nucleus A. (b): Flux measured ($\times 10^{-14} \text{erg s}^{-1} \text{cm}^{-2}$) using a circular aperture of $1''$. Uncertainties 10% - 15%. (c): Internal extinction derived from the $H\alpha/H\beta$ ratio. Error in A_V is 0.5 magnitudes. (d): Average error ± 0.08 (e): Average error ± 0.04 (f): Average error ± 0.05 (g): Average error ± 0.04 . In all cases, emission line ratios are derived using extinction corrected flux values.

TABLE 3
PROPERTIES OF THE REGIONS OF NGC 3690

Reg	Dist ^a (kpc)	$\Delta\alpha^a$ (arcsec)	$\Delta\delta^a$ (arcsec)	$F_{obs}(\text{H}\alpha)^b$	A_V^c (mag)	$\log([\text{OIII}]/\text{H}\beta)^d$	$\log([\text{OI}]/\text{H}\alpha)^e$	$\log([\text{NII}]/\text{H}\alpha)^f$	$\log([\text{SII}]/\text{H}\alpha)^g$
B1	0.00	0.0	0.0	9.7	3.7	0.55	-1.07	-0.29	-0.54
B2	0.49	-1.5	1.9	4.0	3.9	0.43	-1.37	-0.35	-0.74
B11	0.22	0.27	-1.0	5.7	2.0	0.10	-1.37	-0.41	-0.52
B16	0.26	-0.5	-1.1	10.6	1.1	-0.02	-1.68	-0.47	-0.71
B21	0.82	-1.0	3.9	3.1	2.6	0.02	-1.54	-0.48	-0.77
B22	0.63	-2.9	1.0	3.2	2.1	0.02	-1.51	-0.41	-0.68
B25	0.85	-3.9	1.3	7.2	1.7	-0.02	-1.88	-0.47	-0.80
C1	1.83	-2.4	8.6	28.1	3.0	0.13	-1.87	-0.49	-0.96
C2	1.80	-3.0	8.2	33.4	2.1	0.11	-1.92	-0.46	-0.94
C3	1.75	-3.9	7.6	16.7	1.0	0.01	-1.80	-0.44	-0.78
C4	1.39	-4.2	5.3	5.7	0.5	-0.03	-1.80	-0.47	-0.67
C6	1.55	1.0	7.5	5.2	1.9	0.02	-1.74	-0.53	-0.70
C'	1.96	2.7	9.5	0.9	3.8	0.06	-1.40	-0.45	-0.57
D3	1.49	-7.2	-0.9	1.3	1.3	-0.03	-1.60	-0.44	-0.55
D4	1.13	-5.5	0.1	2.6	2.0	-0.05	-1.44	-0.41	-0.57

NOTE. — (a): Distance relative to the nucleus B1. (b): Flux measured ($\times 10^{-14} \text{erg s}^{-1} \text{cm}^{-2}$) using a circular aperture of $0''.9$. Uncertainties 10% - 15% ($\sim 25\%$ for B2). (c): Internal extinction derived from the $\text{H}\alpha/\text{H}\beta$ ratio. Error in A_V is 0.5 magnitudes (0.6 for B1 and C', and ~ 0.7 for B2). (d): Average error ± 0.13 (e): Average error ± 0.13 (f): Average error ± 0.05 (g): Average error ± 0.05 . In all cases, emission line ratios are derived using extinction corrected flux values.

TABLE 4
 $\text{Pa}\alpha/\text{H}\alpha$ -BASED INTERNAL EXTINCTION ESTIMATES

Region	$f(\text{Pa}\alpha)$ ($\times 10^{-15} \text{ erg cm}^{-2} \text{ s}^{-1}$)	$f(\text{Pa}\alpha)/f(\text{H}\alpha)$	A_V (mag)
A	167	5.8	6.1
A1	2.74	0.1	—
A2	5.68	0.2	0.9
A3	4.37	0.2	0.9
A4	9.62	0.3	1.5
A5	8.41	0.1	—
A6	2.73	0.1	—
A7	10.5	0.2	0.9
H1	12.6	0.2	0.9
H2	17.3	0.4	2.0
I	5.11	0.1	—
I1	—	—	—
B1	66.7	0.7	2.8
B2	6.10	0.2	0.9
B11	9.77	0.2	0.9
B16	18.5	0.2	0.9
B21	4.14	0.1	—
B22	5.15	0.2	0.9
B25	11.0	0.2	0.9
C1	85.3	0.3	1.5
C2	76.3	0.2	0.9
C3	10.0	0.1	—
C4	4.70	0.1	—
C6	9.16	0.2	0.9
C'	38.1	4.1	5.6
D3	0.15	0.01	—
D4	4.81	0.2	0.9

NOTE. — Fluxes of $\text{Pa}\alpha$ measured over the selected regions using the HST (F190N-F187N) image. Average uncertainty in A_V is 0.7 magnitudes. Some values are discarded due to the noise affecting $\text{Pa}\alpha$ and $\text{H}\alpha$ low-surface brightness.

TABLE 5
OBSERVED MAGNITUDES AND COLORS

Region	m_{F814W}	m_{F160W}	F110M-F160W	F160W-F222M	F814W-F110M
A	16.85	13.72	1.33	1.36	1.80
A1	18.53	17.59	1.07	1.04	-0.13
A2	18.57	17.36	0.91	0.57	0.30
A3	18.40	17.75	0.81	0.65	-0.15
A4	18.84	18.09	1.05	0.69	-0.31
A5	18.19	17.61	0.72	0.63	-0.14
A6	17.87	17.85	0.70	0.54	-0.68
B1	15.67	13.93	1.23	2.06	0.51
B11	17.30	16.31	0.88	0.64	0.11
B16	16.90	18.12	0.19	—	-1.42
B2	14.09	13.19	0.70	0.69	0.20
B21	16.16	15.35	0.79	0.55	0.03
B22	17.78	16.49	0.93	0.75	0.36
B25	18.01	17.67	0.94	0.62	-0.56
C1	17.04	14.68	1.71	2.67	0.66
C2	16.63	16.57	0.67	—	-0.61
C3	17.04	16.37	0.70	0.52	-0.02
C4	17.24	16.71	0.82	0.44	-0.29
D3	18.74	18.37	0.70	0.46	-0.33

NOTE. — Errors in the colors are ± 0.10 and ± 0.14 for the bright and faint sources respectively.

TABLE 6
PROPERTIES OF THE STELLAR POPULATIONS IN REGIONS OF IC 694 AND NGC 3690

Region	$L(H\alpha)^a$ ($\times 10^{40} \text{ erg s}^{-1}$)	$EW(H\alpha)$ (Å)	Age ($\times 10^6$ years)	$Mass(L_{H\alpha})^b$ ($\times 10^6 M_\odot$)	$Mass(M_{F160W})^c$ ($\times 10^6 M_\odot$)
A	9.2 (150)	201	5.3	40.0 (655.0)	200.0 (460.0)
A1	4.8	217	5.2	17.6	6.0
A2	4.6	292	5.0	13.0	6.4
A3	3.2	297	5.0	9.0	4.8
A4	4.7	382	4.8	10.0	4.0
A5	7.3	307	5.0	21.0	5.3
A6	6.1	197	5.3	26.8	5.0
A7	11.3	277	5.1	36.5	—
F	28.6	760	3.3	21.8	—
G	7.9	654	3.4	6.2	—
H1	18.6	416	4.7	34.0	—
H2	22.5	314	4.9	57.0	—
I	5.8	220	5.2	21.5	—
I1	1.6	86	5.9	12.9	—
B1	62.3*	240*	5.2*	231.0*	200.0*
B2	29.8	22	7.2	678.0	300.0
B11	7.9	200	5.3	34.6	14.0
B16	7.1	311	5.0	20.0	3.1
B21	7.6	62	6.1	74.0	58.0
B22	4.8	138	5.6	27.3	10.0
B25	7.7	449	4.6	13.7	5.6
C1	93.8	680	3.4	74.0	81.0
C2	53.4	645	3.5	43.8	9.8
C3	9.7	440	4.7	17.7	9.8
C4	2.1	156	5.4	10.3	8.4
C6	6.8	609	3.6	5.7	—
C'	5.2 (31.0)	245	5.2	19.0 (115.0)	—
D3	1.0	116	5.7	6.4	3.2
D4	3.6	360	4.8	7.8	—

NOTE. — (a) Luminosity corrected for extinction using $H\alpha/H\beta$ ratio; the extinction using $P\alpha\alpha/H\alpha$ ratio is given for regions A and C' in brackets. (b) Mass derived from the $H\alpha$ luminosity corrected by extinction using $H\alpha/H\beta$ ratio, and assuming the age listed in column 4. In brackets estimate using the $P\alpha\alpha/H\alpha$ extinction-corrected data. (c) Mass derived from the absolute magnitude M_{F160W} corrected by extinction using $H\alpha/H\beta$ ratio, and assuming age listed in column 4. In brackets estimate using the $P\alpha\alpha/H\alpha$ extinction-corrected data. * means AGN contribution.

TABLE 7
KINEMATIC OF THE INTERFACE REGION

Region	$V(\text{H}\alpha)^{\text{a}}$ (km s^{-1})	$V(\text{Na I})^{\text{b}}$ (km s^{-1})	$\sigma(\text{H}\alpha)^{\text{c}}$ (km s^{-1})
K1	-56	-29:	61
K2	-32	—	58
K3	-65	30	80
K4	13	31	68
K5	54	101	35
K6	54	115	20
K7	36	78	30
K8	84	42	70
K9	20	-6:	65
K10	54	86:	100
K11	-2	26	19
K12	-78	—	36

NOTE. — The mean errors for the velocity measurements in $\text{H}\alpha$ and Na I for this bundle are 27 km s^{-1} and 60 km s^{-1} respectively.”:” means large uncertainties. Velocities referred to nucleus (region A) of galaxy IC 694. (a) $V_A(\text{H}\alpha)=3121\pm27 \text{ km s}^{-1}$.(b) $V_A(\text{Na I})=3057\pm34 \text{ km s}^{-1}$. (c) Relative error in σ is $\simeq 13\%$

TABLE 8
KINEMATIC OF IC 694 REGIONS

Region	$V(\text{H}\alpha)^{\text{a}}$ (km s ⁻¹)	$V(\text{Na I})^{\text{b}}$ (km s ⁻¹)	$\sigma(\text{H}\alpha)^{\text{c}}$ (km s ⁻¹)
A	0	0	108
A1	-86	-47	73
A2	-7	22	64
A3	-134	-86	36
A4	-151	-96	50
A5	-67	-25	45
A6	-44	-37	40
A7	-57	-26	41
F	-163	—	72
G	-121	-77	43
H1	-130	-89	61
H2	-117	-93	109
L	60	98	61

11 NOTE. — Velocities referred to nucleus (region A). (a) $V_A(\text{H}\alpha)=3121\pm27$ km s⁻¹. (b) $V_A(\text{Na I})=3057\pm34$ km s⁻¹. (c) Relative error in σ is $\simeq 10\%$

TABLE 9
KINEMATIC OF NGC 3690 REGIONS

Region	$V(\text{H}\alpha)^{\text{a}}$ (km s^{-1})	$V(\text{Na I})^{\text{b}}$ (km s^{-1})	$\sigma(\text{H}\alpha)^{\text{c}}$ (km s^{-1})
B1	0	0	172
B2	-116	-55	110
B11	38	50	143
B16	-46	-15	117
B21	-18	9	128
B22	-121	-48	78
B25	-112	-64	54
C1	32	65	93
C2	16	51	99
C3	13	36	90
C4	-24	8	94
C6	115	—	82
C'	101	—	69
D3	-101	-40	67
D4	-112	-52	54

NOTE. — Velocities referred to nucleus (regions B1). (a) $V_{B1}(\text{H}\alpha)=3040\pm27 \text{ km s}^{-1}$. (b) $V_{B1}(\text{Na I})=2976\pm32 \text{ km s}^{-1}$. (c) Relative error in σ is $\simeq 10\%$

TABLE 10
DYNAMICAL MASS ESTIMATES

Region	R_{eff}^a (kpc)	M_{dyn}^b ($\times 10^9 M_\odot$)
A	0.054–0.062	1.10–1.3
B1	0.035–0.022	1.81–1.1
B2	0.030–0.025	0.63–0.5
C1	0.022–0.042	0.33–0.6
C'	0.023–0.043	0.19–0.3

NOTE. — Dynamical mass estimates for the nuclei of the system (A and B1) and main H α -selected emitting regions (B2, C1 and C'). The stellar and gas effective radius have been derived for the HST F110M (first column) and for F190N (Pa α) (second column). In both cases the dynamical mass has been derived using the H α velocity dispersion values. See §10.3 for details.

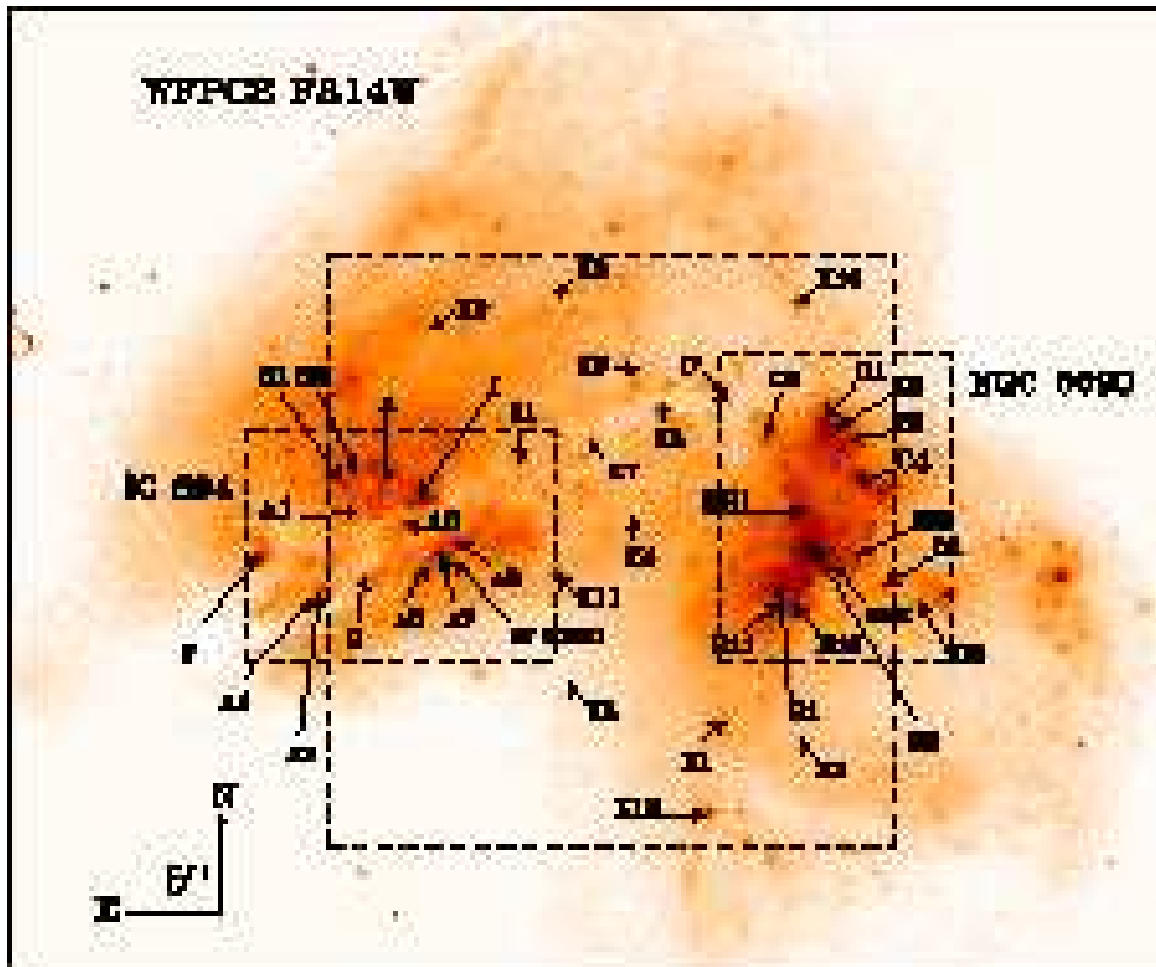


FIG. 1.— Archival HST image of the interacting system Arp 299 obtained with the WFPC2 F814W filter. The rectangular overlays indicate the effective area covered by the three pointings with the two INTEGRAL configurations used (i.e SB2 small rectangles, SB3 large rectangle). We have marked the positions of the regions under study (see § 3 and Tables 1, 2, and 3). The location of the recently discovered near-IR SN is shown too (Mattila et al. 2005). The image is shown on a logarithmic scale. [See the electronic edition of the *Journal* for a color version of this figure.]

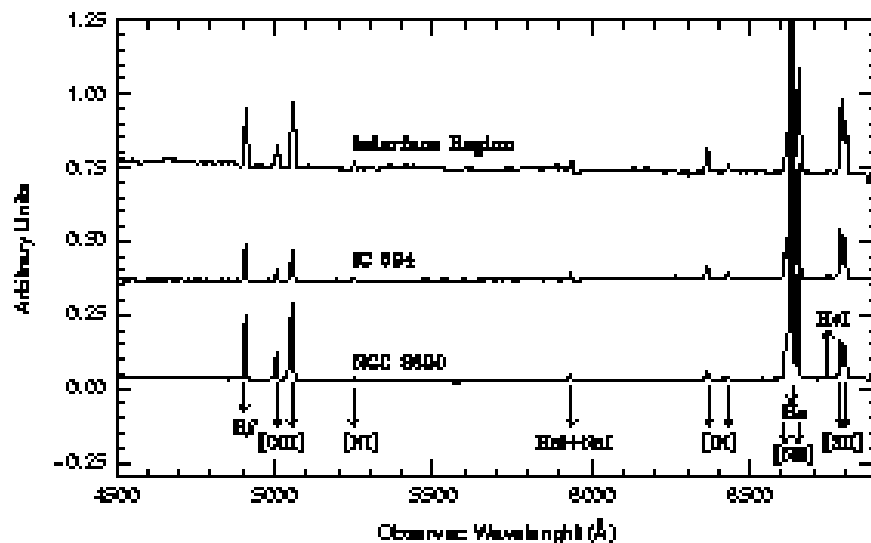


FIG. 2.— Average spectra of the Interface Region (K1 to K12), IC 694 (A, H1 and H2) and NGC 3690 (B1 and B11). The spectral range shown is 4500-6900Å. See Fig. 1 and Tables 1, 2, and 3 for location of the individual emitting sources.

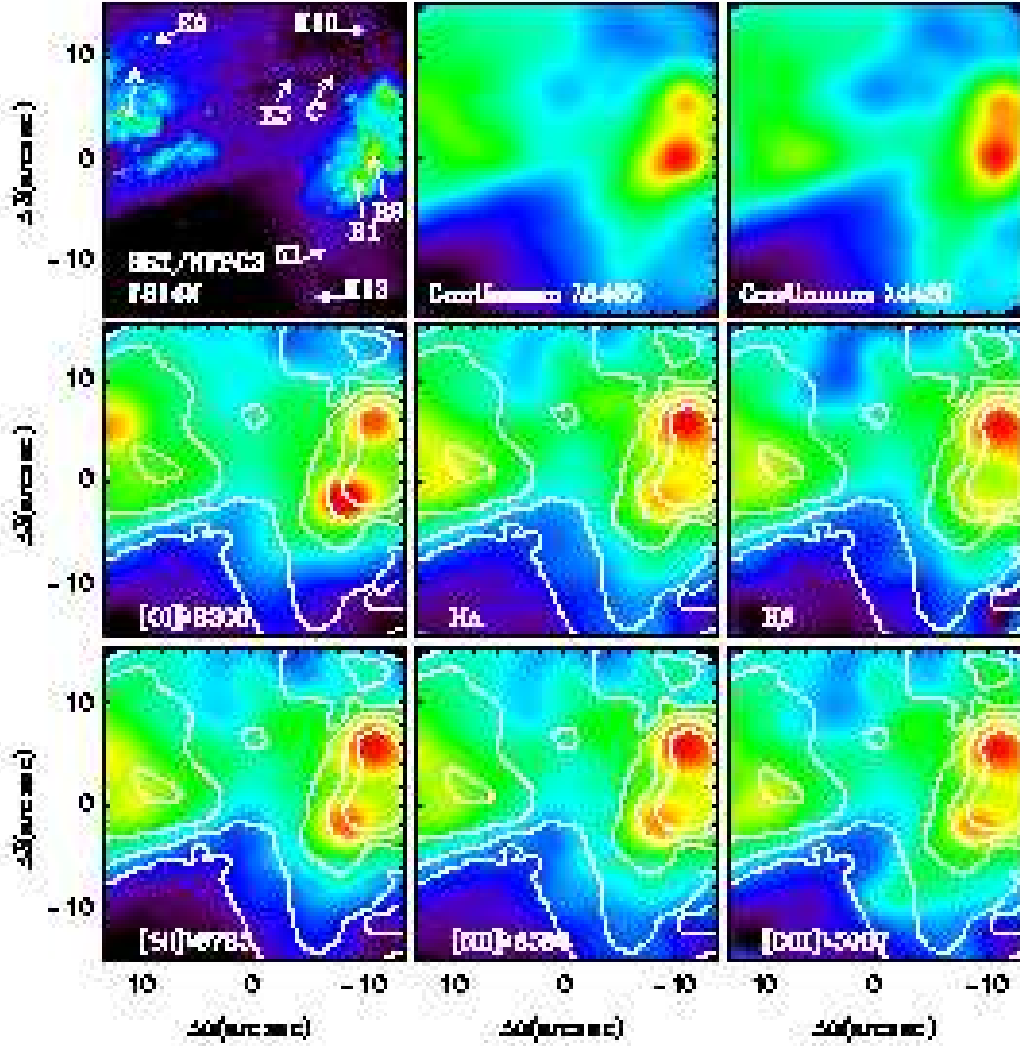


FIG. 3.— Emission-line free stellar continuum and emission line images for Arp 299 obtained with INTEGRAL SB3 bundle. NGC 3690 (B1 and B2) is located to the west and IC 694 (A) to the east. The contours represent the red continuum at $\lambda 6460$. The HST /WFPC2 F814W image is shown for comparison, where several regions of interest discussed in the text are marked. All the images are shown on a logarithmic scale, and the color code represents different intensity levels in each of the individual maps. Orientation is north up, east to the left. [See the electronic edition of the *Journal* for a color version of this figure.]

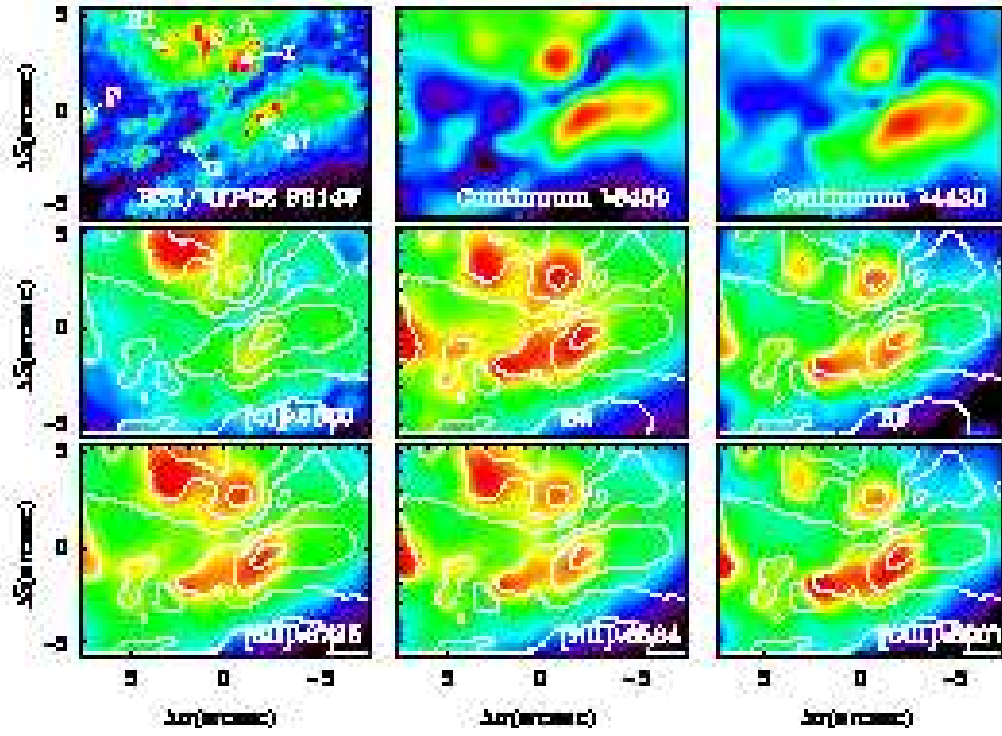


FIG. 4.— Emission-line free stellar continuum and emission line images for IC 694 obtained with INTEGRAL SB2 bundle. The contours represent the red continuum at $\lambda 6460$. The HST/WFPC2 F814W image is also shown for comparison, with several regions of interest marked on it. All the images are shown on a logarithmic scale, and the color code represents different intensity levels in each of the individual maps. Orientation is north up, east to the left. [See the electronic edition of the Journal for a color version of this figure.]

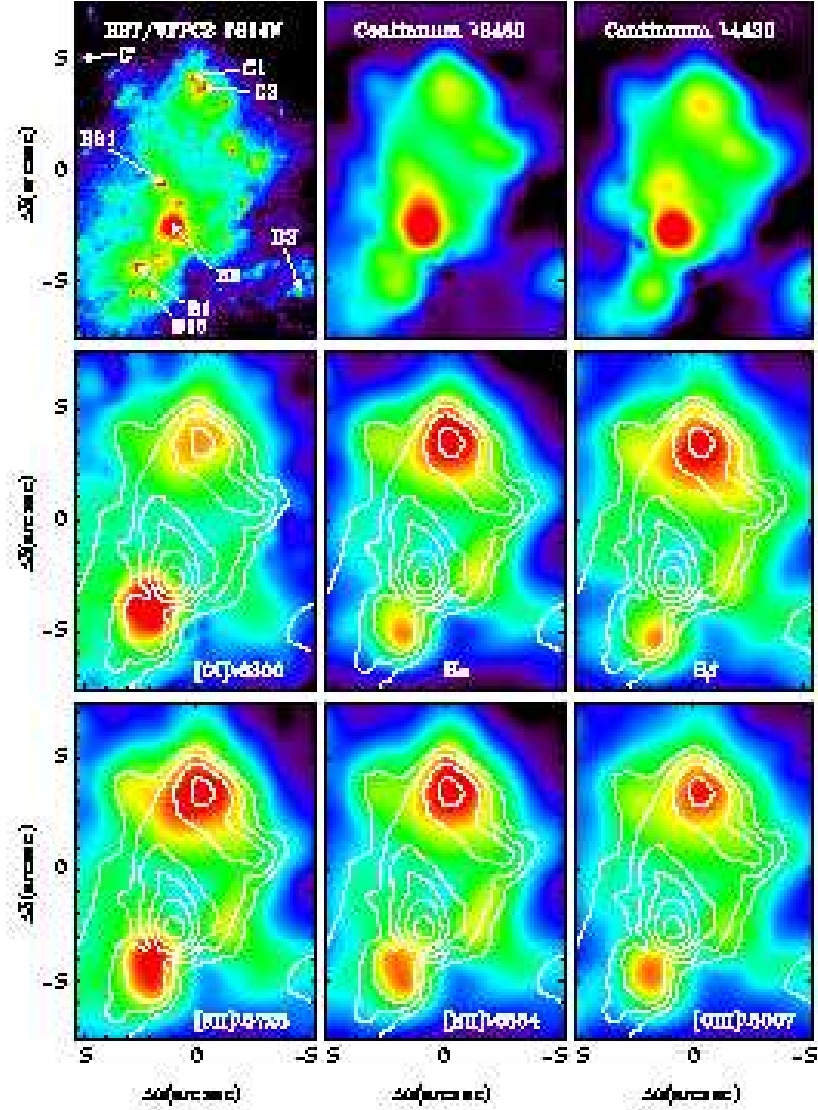


FIG. 5.— Emission-line free stellar continuum and emission line images for NGC 3690 obtained with INTEGRAL SB2 bundle. The contours represent the red continuum at $\lambda 6460$. The HST/WFPC2 F814W image is also shown for comparison, with several regions of interest marked on it. All the images are shown on a logarithmic scale, and the color code represents different intensity levels in each of the individual maps. Orientation is north up, east to the left. [See the electronic edition of the *Journal* for a color version of this figure.]

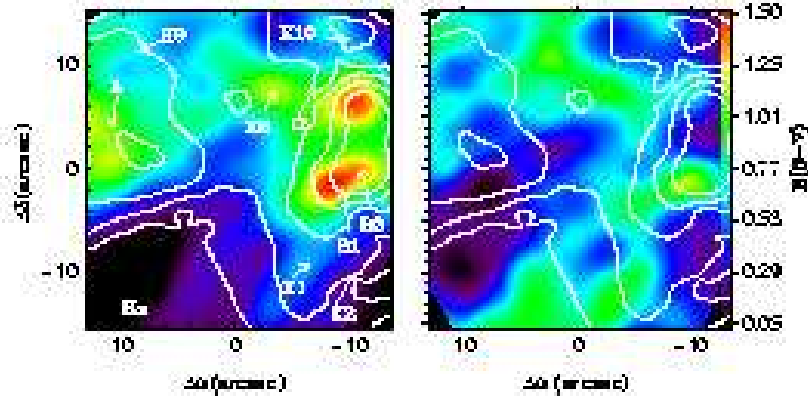


FIG. 6.— *Left panel:* Extinction corrected $H\alpha$ map of the Arp 299 system (including the interface region), shown on a logarithmic scale. *Right panel:* Extinction map of the interface region obtained from the line ratio $H\alpha/H\beta$, shown on a linear scale. Contours are as in Fig. 3. [See the electronic edition of the Journal for a color version of this figure.]

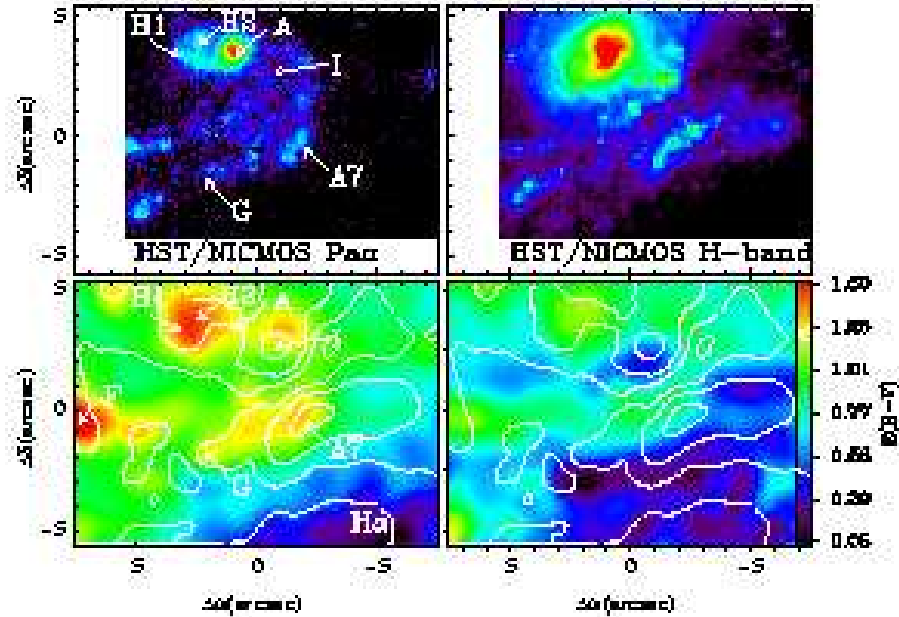


FIG. 7.— IC 694. *Top left panel:* HST/NICMOS continuum subtracted $\text{Pa}\alpha$ emission (F190N-F187N). *Top right panel:* HST/NICMOS H-band continuum. *Bottom left panel:* INTEGRAL $H\alpha$ extinction corrected map. *Bottom right panel:* Extinction map obtained with $H\alpha/H\beta$ line ratio. As a reference several regions in the two fields are marked, and the red continuum contours are superimposed on the interpolated maps. The NICMOS images are shown covering the same FoV as the INTEGRAL data. All the images are shown on a logarithmic scale except for the extinction map, where a linear scale has been applied. [See the electronic edition of the Journal for a color version of this figure.]

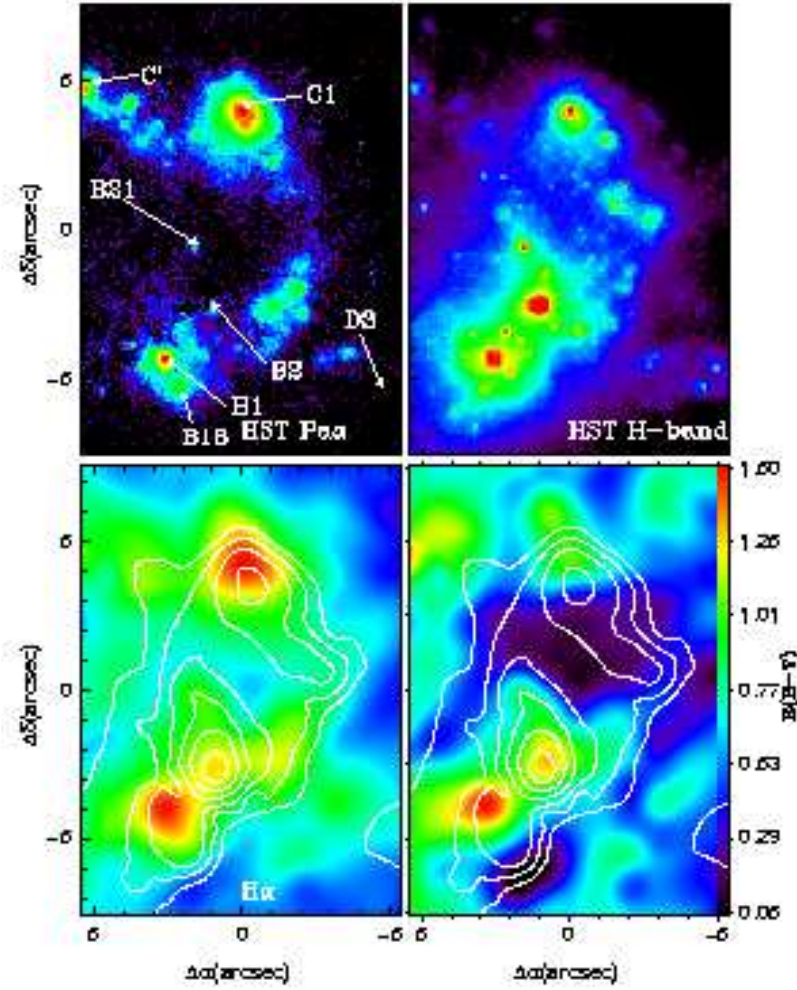


FIG. 8.— NGC 3690. *Top left panel:* HST/NICMOS continuum subtracted Pa α emission (F190N-F187N). *Top right panel:* HST/NICMOS H-band continuum. *Bottom left panel:* INTEGRAL H α extinction corrected map. *Bottom right panel:* Extinction map obtained with H α /H β line ratio. As a reference several regions are marked, and the red continuum contours are superimposed on the interpolated maps. The NICMOS images are shown covering the same FoV as the INTEGRAL data. All the images are shown on a logarithmic scale except for the extinction map, where a linear scale has been applied. [See the electronic edition of the Journal for a color version of this figure.]

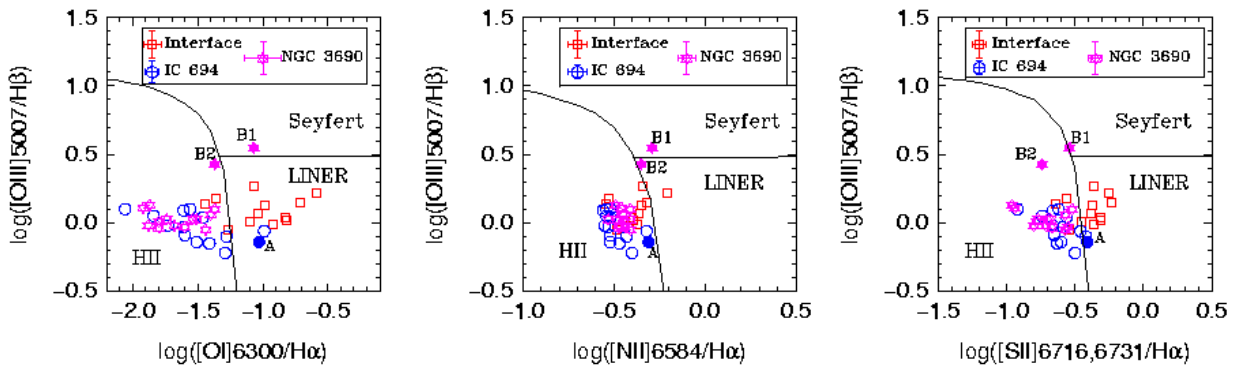


FIG. 9.— Optical emission line diagnostic diagrams for the studied regions of Arp 299. Filled symbols represent nuclei A and B1, and region B2. Note that B1, as observed with the SB2 bundle, is classified as Seyfert according to these diagrams. The open symbols are the regions given in Tables 1, 2, and 3. Typical uncertainties in the line ratios of each individual galaxy are shown. [See the electronic edition of the Journal for a color version of this figure.]

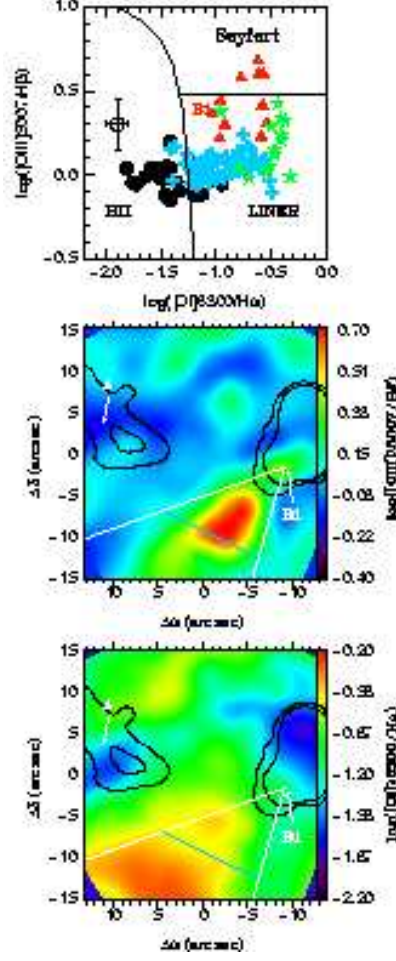


FIG. 10.— Diagnostic diagram and line ratio maps derived from INTEGRAL/SB3 data. *Upper panel:* Diagnostic diagram with all the data from the SB3 bundle displayed. The symbol code is as follows: triangles represent values within the ionization cone, and at a distance of less than 2 kpc from B1. Stars represent the zone within the cone at distances of 2 to 4 kpc from B1. Crosses mark the rest of the regions in the interface. Filled circles represent regions in IC 694 and NGC 3690 (defined as the regions within the iso-contours). B1 has been included in the ionization cone, and labeled as a triangle. *Center panel:* $[\text{O III}]\lambda 5007/\text{H}\beta$ map. Nuclei A and B1 are marked. The white lines indicate the ionization cone. The transversal line to the axis of the cone separates the inner (with Seyfert-like regions) and outer (LINER-like) sections of the cone. *Lower panel:* $[\text{O I}]\lambda 6300/\text{H}\alpha$ map. The labels and overlays as in the center panel. [See the electronic edition of the Journal for a color version of this figure.]

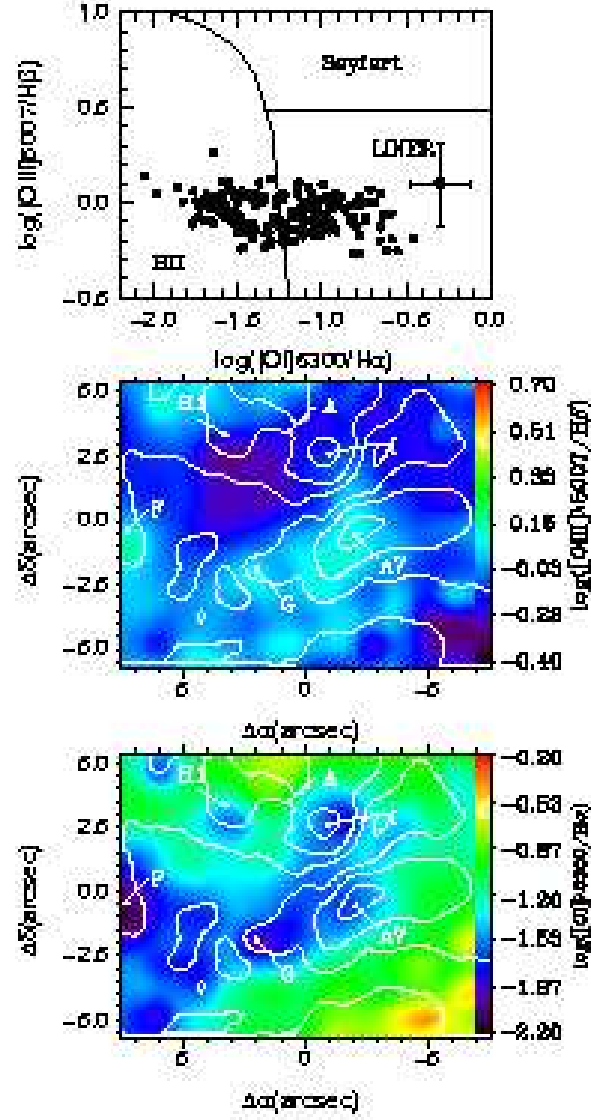


FIG. 11.— Emission line diagnostic diagram and excitation maps based on line ratios for IC 694. *Upper panel:* Diagnostic diagram obtained for the individual SB2 spectra. *Center and Lower panels:* Diagnostic maps derived from reconstructed emission line maps. As a reference we have marked several regions and superimposed red continuum contours. [See the electronic edition of the *Journal* for a color version of this figure.]

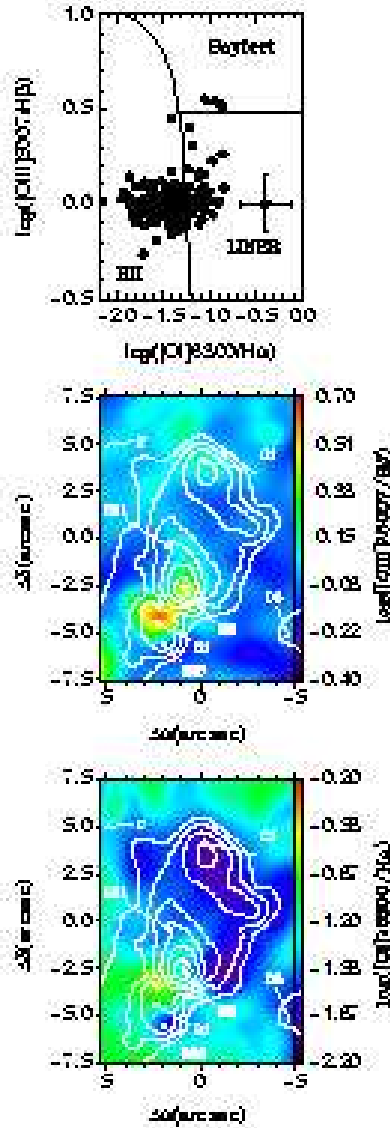


FIG. 12.— Emission line diagnostic diagram and excitation maps based on line ratios for NGC 3690. *Upper panel:* Diagnostic diagram obtained from the individual SB2 spectra. *Center and Lower panels:* Diagnostic maps derived from reconstructed emission line maps. As a reference we have marked several regions and superimposed red continuum contours. [See the electronic edition of the *Journal* for a color version of this figure.]

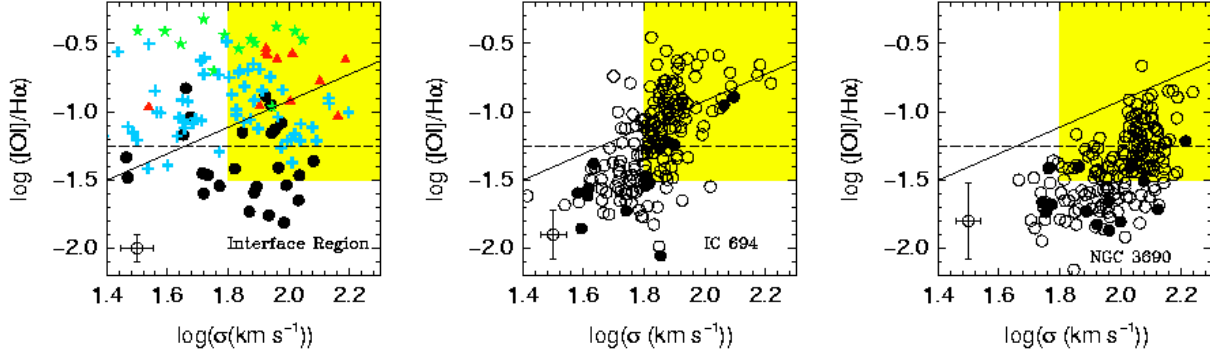


FIG. 13.— Relation between velocity dispersion and $[\text{O I}]\lambda 6300/\text{H}\alpha$ ratio for the three INTEGRAL pointings, i.e. interface region (*Left*), IC 694 (*Center panel*) and NGC 3690 (*Right panel*). In all cases the relation derived by Monreal-Ibero et al. (2006) for a set of ULIRGs is shown (solid line). The shaded area indicate the region covered by extra-nuclear regions of ULIRGs (Monreal-Ibero et al. 2006). The horizontal dashed line marks the average values separating H II and LINER-like ionization. *Left panel:* The symbol code as in Fig. 10. *Center and Right panels:* Filled symbols indicate the fibers of the studied individual regions listed in Tables 2 and 3. [See the electronic edition of the Journal for a color version of this figure.]

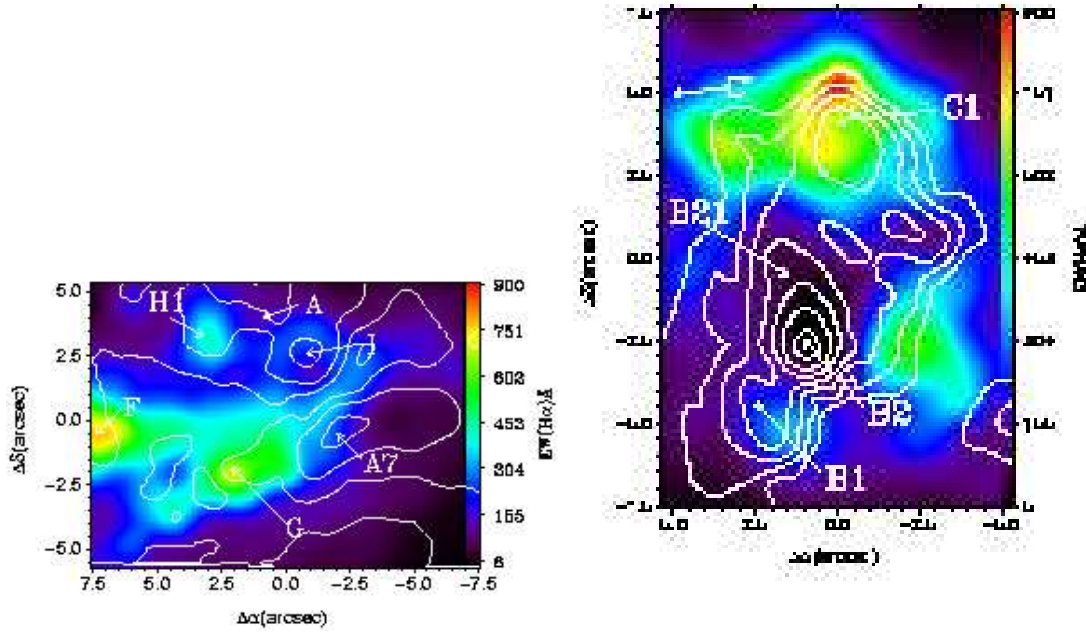


FIG. 14.— H α equivalent width maps. Orientation is north up, east to the left. *Left panel:* IC 694. *Right panel:* NGC 3690. Note that nuclei A and B1 have low equivalent widths. [See the electronic edition of the Journal for a color version of this figure.]

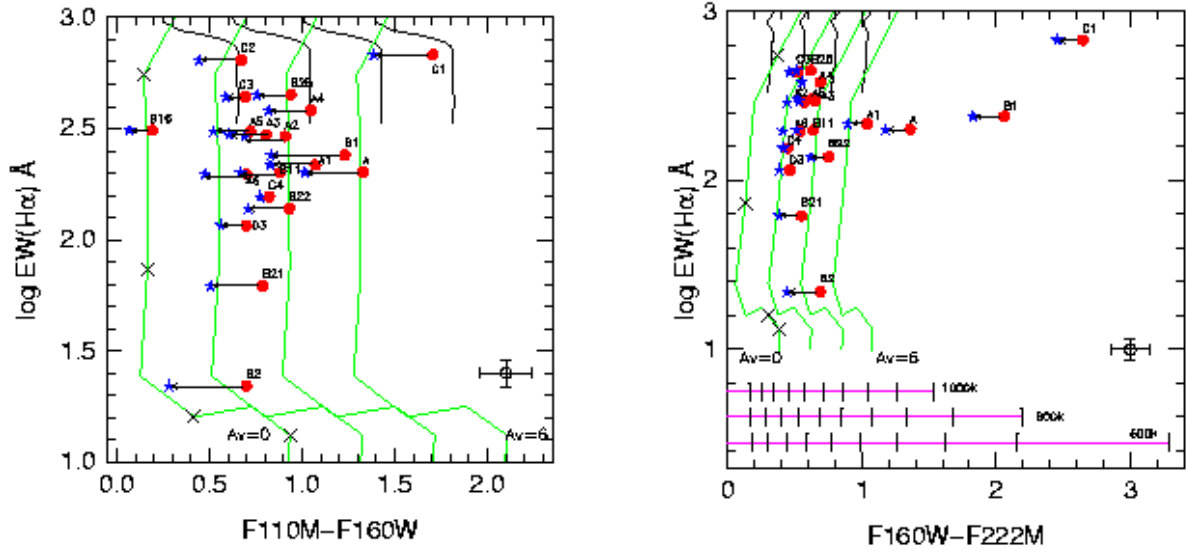


FIG. 15.— Plots representing the results of the stellar evolutionary models (SB99, Geneva High Isochrones, Salpeter IMF, using upper and lower mass boundaries of 0.1 and 100 M_{\odot}) compared with the measured values. The long tracks represent the evolution of instantaneous bursts as a function of age (from top to bottom, black crosses mark 4, 6, 8 and 10 Myr). Short tracks correspond to continuous bursts using a SFR of 1 M_{\odot} year $^{-1}$. In both cases from left to right the extinction ranges from $A_V=0$ to $A_V=6$, in steps of 2 magnitudes. The filled circles are the measured values, and the stars represent the extinction corrected values from the $H\alpha/H\beta$ ratio. *Left panel:* F110M-F160W color vs $H\alpha$ equivalent width. *Right panel:* F160W-F222M color vs $H\alpha$ equivalent width. The long horizontal lines represent the colors expected from a extinction-free stellar population of 6×10^6 years with an increasing K-band flux contribution of hot dust at different temperatures (from 0% to 100%, increasing 10% on each step). In both cases nucleus B1 is included for completeness. [See the electronic edition of the Journal for a color version of this figure.]

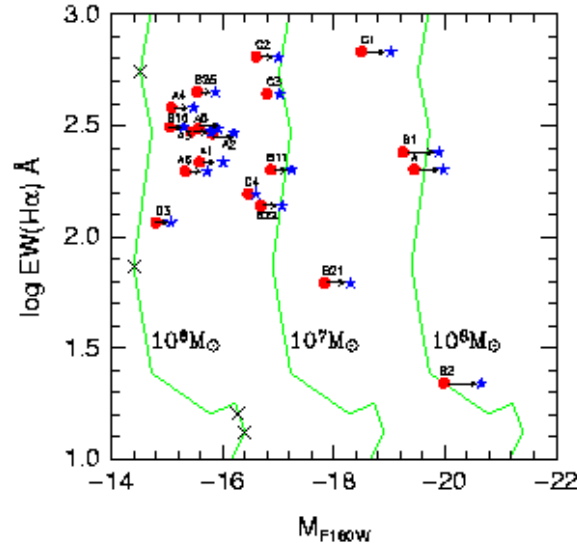


FIG. 16.— Results of the stellar evolutionary models (SB99, Geneva High Isochrones, Salpeter IMF, using upper and lower mass boundaries of 0.1 and 100 M_{\odot}) compared with measured values. Long tracks are the output for instantaneous bursts as a function of age (from top to bottom, black crosses mark 4, 6, 8 and 10 Myr), and different cluster mass. The filled circles represents measured absolute F160W magnitude, and the stars represent the extinction corrected values from the $H\alpha/H\beta$ ratio. [See the electronic edition of the Journal for a color version of this figure.]

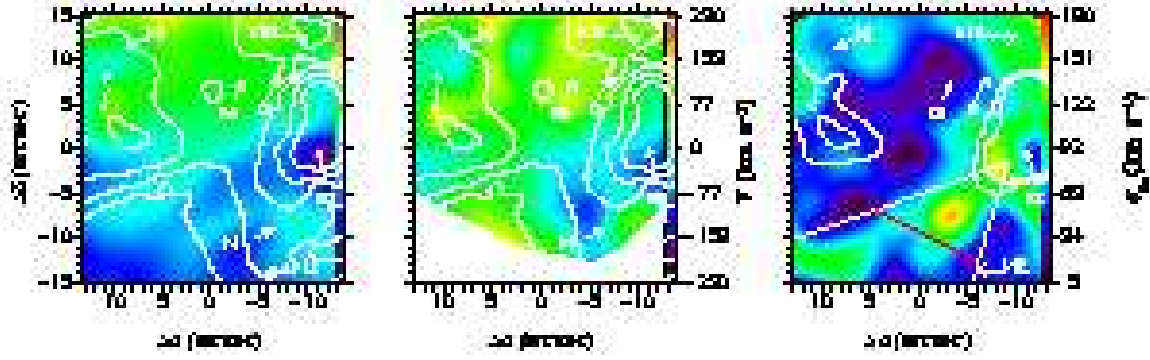


FIG. 17.— Arp 299 interface region kinematics. Velocity field of the ionized gas as traced by the $H\alpha$ line (*Left panel*), neutral gas as traced by the Na I line (*Center panel*) and velocity dispersion of the ionized gas (*Right panel*). The velocities are referred to the nucleus A as observed with the higher spatial resolution SB2 bundle, i.e. $3121 \pm 27 \text{ km s}^{-1}$ for the ionized and $3057 \pm 34 \text{ km s}^{-1}$ for the neutral gas. Lines depicted the ionization cone as in Fig 10. [See the electronic edition of the Journal for a color version of this figure.]

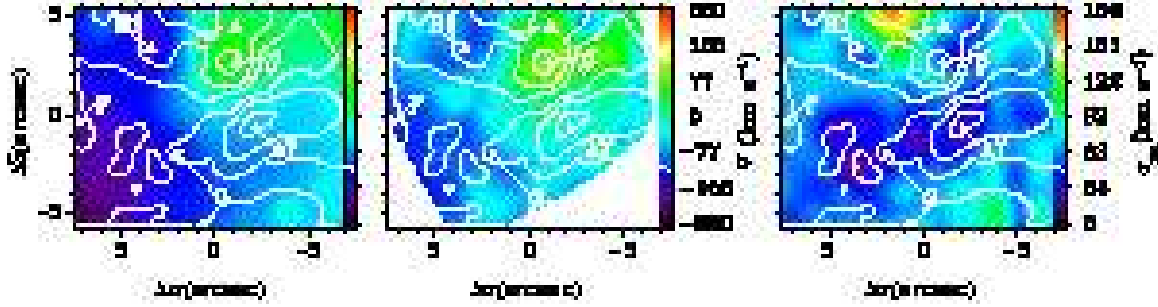


FIG. 18.— IC 694 kinematics. Velocity field of the ionized gas as traced by the $H\alpha$ line (*Left panel*), neutral gas as traced by the Na I line (*Center panel*) and velocity dispersion of the ionized gas (*Right panel*). The velocities are referred to the nucleus A, for which the ionized gas velocity is $3121 \pm 27 \text{ km s}^{-1}$ and the neutral gas velocity is $3057 \pm 34 \text{ km s}^{-1}$. [See the electronic edition of the Journal for a color version of this figure.]

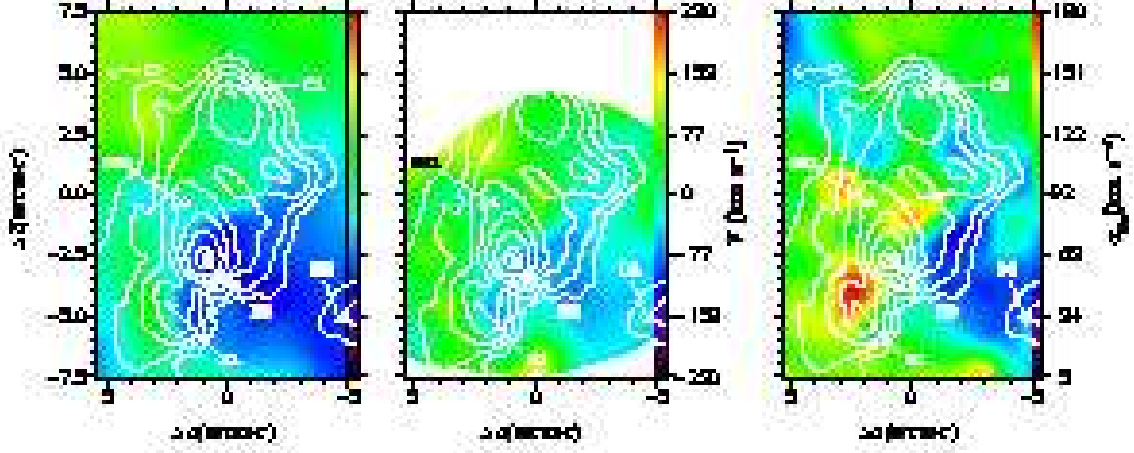


FIG. 19.— NGC 3690 kinematics. Velocity field of the ionized gas as traced by the $H\alpha$ line (*Left panel*), neutral gas as traced by the Na I line (*Center panel*) and velocity dispersion of the ionized gas (*Right panel*). The velocities are referred to the nucleus B1, for which the ionized gas velocity is 3040 ± 27 km s $^{-1}$ and the neutral gas velocity is 2976 ± 32 km s $^{-1}$. Note that the nucleus B1 presents the the highest σ value. [See the electronic edition of the *Journal* for a color version of this figure.]